DRP1-mediated mitochondrial fission is essential to maintain cristae morphology and bioenergetics

Gabriella L. Robertson[1], Stellan Riffle[1], Mira Patel[1], Andrea Marshall[2], Heather Beasley[2], Edgar Garza Lopez[2], Jianqiang Shao[3], Zer Vue[2], Maria S. Stoll[4], Sholto de Wet[5], Rensu P. Theart[6], Ben Loos[6], Antentor Hinton Jr.[2], Jason A. Mears[4], and Vivian Gama[1,7,8,9]

[1]Vanderbilt University, Cell and Developmental Biology, Nashville, TN.
[2]Vanderbilt University, Molecular Physiology and Biophysics, Nashville, TN.
[3]Central Microscopy Research Facility, University of Iowa, Iowa City, IA.
[4]Case Western Reserve University, Department of Pharmacology and Center for Mitochondrial Diseases, Cleveland, OH.
[5]Stellenbosch University, Department of Physiological Sciences, Stellenbosch, South Africa
[6]Stellenbosch University, Department of Electrical and Electronic Engineering, Stellenbosch, South Africa
[7]Vanderbilt University, Vanderbilt Center for Stem Cell Biology, Nashville, TN
[8]Vanderbilt University, Vanderbilt Brain Institute, Nashville, TN

[9]Corresponding author

Correspondence should be addressed to:

Vivian Gama
PMB407935
465 21st Avenue South, 4150A
Vanderbilt University
Nashville, TN 37240-7935
Tel: (615) 875-9490
vivian.gama@vanderbilt.edu

Running title: DRP1 mutations associated with EMPF1

Keywords: fibroblasts, DRP1, mitochondria, peroxisomes, cristae, glycolysis, oxidative phosphorylation

Abstract

Mitochondria and peroxisomes are both dynamic signaling organelles that constantly undergo fission. While mitochondrial fission is known to coordinate cellular metabolism, proliferation, and apoptosis, the physiological relevance of peroxisome dynamics and the implications for cell fate are not fully understood. DRP1 (dynamin-related protein 1) is an essential GTPase that executes both mitochondrial and peroxisomal fission. Patients with *de novo* heterozygous missense mutations in the gene that encodes DRP1, *DNM1L (Dynamin 1 Like)*, present with encephalopathy due to defective mitochondrial and peroxisomal fission (EMPF1). EMPF1 is a devastating neurodevelopmental disease with no effective treatment. To interrogate the mechanisms by which DRP1 mutations cause cellular dysfunction, we used human-derived fibroblasts from patients with mutations in DRP1 who present with EMPF1. As expected, patient cells display elongated mitochondrial morphology and lack of fission. Patient cells display a lower coupling efficiency of the electron transport chain, increased proton leak, and upregulation of glycolysis. In addition to these metabolic abnormalities, mitochondrial hyperfusion results in aberrant cristae structure and hyperpolarized mitochondrial membrane potential, both of which are tightly linked to the changes in metabolism. Peroxisome structure is also severely elongated in patient cells and results in a potential functional compensation of fatty acid oxidation. Understanding the mechanism by which DRP1 mutations cause these metabolic changes will give insight into the role of mitochondrial dynamics in cristae maintenance and the metabolic capacity of the cell, as well as the disease mechanism underlying EMPF1.

Introduction

Mitochondrial dynamics are controlled and executed by a vast group of proteins and other organelles. The underlying morphology of the mitochondria is an important determinant for the

59 ability of this organelle to regulate a variety of cellular processes, such as apoptosis, cell fate, lipid
60 biosynthesis, and epigenetic modifications (Bayraktar et al., 2019; Iwata et al., 2020; Khacho et
61 al., 2016; King et al., 2021; Prigione and Adjaye, 2011; Rasmussen et al., 2020; Vantaggiato et
62 al., 2019). Mitochondrial fusion is primarily catalyzed by the large GTPases Mitofusin 1 and
63 Mitofusin 2 at the outer mitochondrial membrane (Chen et al., 2003). The GTPase OPA1 (Optic
64 Atrophy 1) is responsible for executing fusion of the inner mitochondrial membrane (Alexander et
65 al., 2000; Delettre et al., 2000). Mitochondrial fission, mediated through the large GTPase DRP1
66 (Dynamin-related protein 1), is orchestrated by a complex sequence of events (Fonseca et al.,
67 2019; Smirnova et al., 2001). The first steps of mitochondrial fission include contact with the
68 endoplasmic reticulum (ER) and replication of the mitochondrial genome (Friedman et al., 2011;
69 Lewis et al., 2016). This is followed by contact and pre-constriction by actin filaments, which are
70 associated with the ER membrane (Chakrabarti et al., 2018; Hatch et al., 2016, 2014; Ji et al.,
71 2017, 2015; Li et al., 2015). Fission is also regulated through adaptor proteins at the outer
72 mitochondrial membrane, including MiD49 (Mitochondrial Dynamics Protein 49), MiD51
73 (Mitochondrial Dynamics Protein 51), MFF (Mitochondrial Fission Factor), and FIS1 (Fission,
74 Mitochondrial 1), however, their distinct roles in fission are not completely understood (Losón et
75 al., 2013; Osellame et al., 2016; Palmer et al., 2013). After the association with adaptor proteins,
76 DRP1 then forms a multimeric ring around the mitochondria and hydrolyzes GTP to GDP causing
77 a confirmational change in the ring that executes fission (Chang and Blackstone, 2007; Fröhlich
78 et al., 2013; Nagashima et al., 2020). DRP1 is essential for mitochondrial fission and without
79 functional DRP1, the mitochondrial network becomes hyperfused. In addition to the effects on
80 mitochondrial morphology, DRP1 also mediates the fission of peroxisomes (Koch et al., 2003).
81 Peroxisomes are highly specialized organelles vital for the beta oxidation of very-long-chain fatty
82 acids, detoxification of reactive oxygen species (ROS), production of cholesterol, bile acids, and
83 plasmalogens, which contribute to the phospholipid content in the brain white matter (Chandel,
84 2021; Ding et al., 2021; Ferreira et al., 2021; Lodhi and Semenkovich, 2014; Ravi et al., 2021;

85 Schrader et al., 2020; Sugiura et al., 2017). The adaptor proteins MFF and FIS1 are also involved
86 in DRP1 recruitment to sites of peroxisome fission (Gandre-Babbe and Van Der Bliek, 2008;
87 Itoyama et al., 2013; Koch and Brocard, 2012). The contacts between mitochondria and
88 peroxisomes are essential for linking peroxisomal β-oxidation and mitochondrial ATP generation
89 by the electron transport chain (ETC), maintenance of redox homeostasis, and lipid transfer
90 (Chandel, 2021; Fan et al., 2016; Fransen et al., 2017). Thus, peroxisomal and mitochondrial
91 metabolic activities are functionally interconnected. Consistent with this, peroxisomal disorders
92 caused by mutations in genes involved in the biogenesis and function of peroxisomes, are often
93 associated with mitochondrial dysfunction (Tanaka et al., 2019). This communication may be
94 particularly important during brain development and metabolic stress. However, the molecular
95 mechanisms that facilitate this communication are still poorly understood.

96 In mouse models, global DRP1 knockout is embryonic lethal (Ishihara et al., 2009; Wakabayashi
97 et al., 2009). With the advent of exome sequencing, patients with *de novo* mutations in the gene
98 that encodes DRP1, *DNM1L (Dynamin 1 Like)*, have been identified (Chao et al., 2016; Fahrner
99 et al., 2016; Keller et al., 2021; Liu et al., 2021; Longo et al., 2020; Nasca et al., 2016; Nolan et
100 al., 2019; Ryan et al., 2018; Sheffer et al., 2016; Vandeleur et al., 2019; Waterham et al., 2007;
101 Yoon et al., 2016). The disease associated with mutations in *DNM1L* is known as encephalopathy
102 due to defective mitochondrial and peroxisomal fission-1 (EMPF1) (OMIM 614388). Most reported
103 mutations are heterozygous missense mutations. Patients present with heterogeneous symptoms
104 including neurodevelopmental delay, seizures, muscle abnormalities, and ataxia. Patient
105 fibroblasts show very elongated mitochondrial networks and elevated lactate levels, suggesting
106 an impairment in oxidative phosphorylation (Liu et al., 2021; Whitley et al., 2018). Currently, there
107 is no effective treatment or cure for patients effected by DRP1 mutations. The life expectancy for
108 most patients with DRP1 mutations is childhood to early adolescence (Ryan et al., 2018).
109 Although other proteins and organelles are involved in fission, DRP1 has been shown to be

110 indispensable for mitochondrial fission (Csordás et al., 2006; Fonseca et al., 2019; Kamerkar et
111 al., 2018; Li et al., 2015; Nagashima et al., 2020; Smirnova et al., 2001), yet the cellular
112 consequences of DRP1 dysfunction are not well understood. In this study, we aimed to
113 characterize the effects of two DRP1 mutations identified in patients with EMPF1, the G32A
114 mutation, which lies in the catalytic GTPase domain of DRP1, and the R403C mutation, which
115 lies in the stalk domain (Fröhlich et al., 2013) (Figure 1A), on mitochondrial network morphology,
116 cristae ultrastructure, and related metabolic adaptations, to gain fundamental insight into the
117 cellular adaptations to dysfunctional organelle fission and the pathophysiology of EMPF1.

118 Here, we resolve and quantify mitochondrial and peroxisomal morphological features associated
119 with EMPF1-associated mutations and reveal their impact on cellular metabolism, to put into
120 perspective the clinical findings that were previously described (Fahrner et al., 2016; Liu et al.,
121 2021; Ryan et al., 2018). We found that the inability of DRP1 to fragment the mitochondria in
122 patient-derived fibroblasts leads not only to the hyperfusion phenotype previously described, but
123 also to delayed cell death in response to apoptotic signals, aberrant mitochondrial cristae
124 structure, and hyperpolarized mitochondrial membrane potential. Metabolically, the changes in
125 mitochondrial and peroxisomal morphology result in inefficiency of ETC coupling oxygen
126 consumption with ATP production and upregulation of glycolysis. Altogether, these data indicate
127 that mitochondrial and peroxisomal fission influence dynamics of the inner mitochondrial
128 membrane and the metabolic state of the cell.

129

130 **Results**

131 **DRP1 variants found in patients have dominant negative effects that alter the expression**
132 **of critical proteins at the mitochondria**

133 Light microscopy studies have shown the profound alterations of mitochondrial fission in cells
134 from patients harboring mutations in DRP1 (Ryan et al., 2018; Whitley et al., 2018). These studies
135 highlighted the clinical relevance of mitochondrial fission in neural development. We quantified
136 the morphology of the mitochondria in patient-derived primary fibroblasts at super resolution level
137 using structured illumination microscopy (SIM). Both patient fibroblast lines showed increased
138 mitochondrial volume, surface area and major axis length, consistent with a hyperfused
139 mitochondrial morphology, as reported for DRP1 null cells (Fonseca et al., 2019; Kamerkar et al.,
140 2018; Smirnova et al., 2001) (Fig. 1B-C). Live-cell imaging of mitochondria stained with
141 MitoTracker confirmed that mitochondrial fission events are rare in patient cells compared to
142 control fibroblasts (Supplementary Fig. 1A). High resolution three-dimensional images of control
143 and patient fibroblasts were obtained using serial block facing-scanning electron microscopy
144 (SBF-SEM) (Garza-Lopez et al., 2021). Manual segmentation and stack reconstruction of the
145 mitochondrial networks validated the increased length and volume of the mitochondrial networks
146 as well as increased mitochondrial complexity index (MCI) in patient fibroblasts (Fig. 1D-E). MCI
147 is a quantitative measurement of network complexity, which takes into account both volume and
148 surface area of the mitochondria (MCI = $SA^3 / 16\pi^2V^2$) (Faitg et al., 2021; Vincent et al., 2019).
149 Both mutations in DRP1 result in significant alterations of the mitochondrial network with G32A
150 fibroblasts showing slightly more severe elongation than R403C (Fig. 1E and Supplementary Fig.
151 1B).

152 Both mutations in DRP1 are found to be heterozygous in patients, suggesting that mutant DRP1
153 has a dominant effect that can interfere with the ability of wild-type DRP1 to fragment the
154 mitochondria. To test this, we generated mCherry tagged- constructs containing the patient
155 derived mutations and expressed them in human fibroblasts homozygous for endogenous wild-
156 type DRP1. Overexpression of mCherry-DRP1-G32A and mCherry-DRP1-R403C by transient
157 transfection in wild-type fibroblasts demonstrated that, as previously described (Montecinos-

158 Franjola et al., 2020, Fahrner et al., 2016; Ryan et al., 2018; Whitley et al., 2018), the
159 mitochondrial hyperfusion seen in patient cells is not due to the genetic background and that these
160 mutations act in a dominant negative manner (Fig. 1F-G). While both mutations of DRP1
161 significantly impaired DRP1 function in human fibroblasts, the G32A show a slightly more severe
162 phenotype than R403C.

163 Hyperfusion of the mitochondrial membrane due to sequestration and inactivation of DRP1 is
164 thought to lead to unopposed fusion events that increase the severity of mitochondrial elongation
165 (Palmer et al., 2013). We examined the effects of DRP1 mutations on the protein expression
166 levels of mitochondrial dynamics proteins. Both Mitofusin 1 and Mitofusin 2 were expressed at
167 lower levels in patient cells than in control cells. However, there was no significant difference in
168 the expression of OPA1 (Fig. 2A). These data show that there is a reduction in the expression of
169 mitochondrial outer membrane fusion proteins in patient cells, suggesting that active
170 mitochondrial fission promotes protein stability at the outer mitochondrial membrane and
171 compensatory fusion events.

172 Phosphorylation of DRP1 at Serine 616 has been proposed to be a critical determinant of DRP1
173 recruitment and activity (Koch and Brocard, 2012; Taguchi et al., 2007; Valera-Alberni et al.,
174 2021). Whether mutations in DRP1 found in patients with EMPF1 affect the levels of
175 phosphorylation at Serine 616 has not been explored. We examined DRP1 levels in patient
176 derived fibroblasts. Although there was no significant difference in total DRP1 expression, G32A
177 patient cells expressed significantly less pS616-DRP1 than control cells (Fig. 2B). Since G32A
178 mutation impairs DRP1 phosphorylation to a greater extent than the R403C mutation, the GTPase
179 domain of DRP1 may be structurally or functionally involved in DRP1 phosphorylation. We
180 wondered whether the expression of one copy of mutant DRP1 in patient fibroblasts affected the
181 recruitment of endogenous pS616-DRP1 to the mitochondria. To test this, we quantified the
182 recruitment of phosphorylated DRP1 to the outer mitochondrial membrane using super-resolution

183 microscopy. On average, there was no significant difference in the recruitment of pS616-DRP1 to
184 the mitochondria in patient cells and control cells (Fig. 2C-D). While in all cell lines, pS616-DRP1
185 was found in close contact to the mitochondrial membrane, in the patient fibroblasts this
186 interaction appeared less transient. These results point to generalized stalling of the fission events
187 in patient fibroblasts.

188 The onset of apoptosis is accompanied by mitochondrial remodeling, stable association of DRP1
189 to the mitochondrial membrane, and increased fragmentation of the mitochondrial membrane
190 (Martinou and Youle, 2006; Wasiak et al., 2007). In DRP1 deficient cells, this remodeling of
191 mitochondria is significantly reduced and the onset of cell death is delayed (Lee et al., 2004). To
192 determine the effects of mitochondrial stress on mitochondrial fragmentation in patient fibroblasts,
193 we quantified changes in mitochondrial fission in response to CCCP treatment. As previously
194 shown using RNAi experiments in HeLa cells, patient fibroblasts showed reduced mitochondrial
195 fragmentation induced by CCCP compared to control cells (Fig. 2E-F). Although some
196 mitochondrial fragmentation may occur, mitochondrial volume and major axis length are
197 significantly larger in patient cells treated with CCCP than control cells. Upon apoptosis, BAX
198 translocates to the mitochondria and cytochrome *c* is released to the cytosol (Smaili et al., 2001).
199 While in DRP1 depleted cells BAX is recruited to the mitochondria, cytochrome *c* release is
200 delayed. Consistent with this, patient fibroblasts show higher cell survival when treated with CCCP
201 and Etoposide; as well as, lower caspase-3 activity than control fibroblasts when treated with STS
202 (Supplementary Fig. 2A-B). Interestingly, basal levels of both BAX and BAK are significantly
203 reduced in patient fibroblasts with mutations in DRP1 (Supplementary Fig. 2C). Levels of the anti-
204 apoptotic protein MCL-1 were significantly reduced in G32A fibroblasts but not in R403C
205 fibroblasts, while BCL-XL expression levels remained relatively constant in all cell lines. Thus,
206 patient fibroblasts may display a compensatory adaptation to reduce the basal levels of BAX/BAK
207 activation. Whether this reduction in the ability to undergo apoptosis in response to mitochondrial

208 stress is a widespread phenomenon in all tissues of EMPF1 patients and/or whether apoptosis
209 inhibition results in deleterious accumulation of mitochondrial and nuclear DNA encoded
210 mutations remains unexplored. No significant alteration in the protein expression of DRP1
211 adaptors was detected (Supplementary Fig. 2D).

212 **Mitochondrial hyperfusion in DRP1 mutant fibroblasts leads to higher glycolytic rate and**
213 **increased mitochondrial membrane potential**

214 Mitochondrial morphology is tightly linked to metabolic function (Dorn, 2015; Wai and Langer,
215 2016); thus, we assessed the effects of DRP1 patient mutations on cellular metabolism by
216 measuring rates of glycolysis and oxidative phosphorylation (OXPHOS) in cells using the
217 sensitive high-throughput Seahorse XF Analyzer. The Seahorse analyzer measures extracellular
218 oxygen consumption as a readout of OXPHOS and extracellular acidification as a readout of
219 glycolysis. Basal and maximal oxygen consumption was not significantly different in mutant cells
220 compared to control, suggesting no major defects in ATP production (Fig. 3A). However, proton
221 leak was significantly higher in the G32A patient cells and coupling efficiency was significantly
222 lower in both patient lines (Fig. 3B). Therefore, although basal ATP production is not perturbed in
223 the mutant cells, the ETC is not effectively coupling substrate oxidation and ATP synthesis.
224 Extracellular acidification rate was significantly increased in both patient lines, consistent with an
225 upregulation of glycolysis (Fig. 3A) and the hyperlactacidemia observed in more than 50% of
226 patients with mutations in DRP1 (Liu et al., 2021). A glycolytic rate assay confirmed that both
227 basal and compensatory glycolysis are higher in both patient lines (Fig. 3C). Thus, although the
228 cells are capable of producing ATP, DRP1 mutations cause a defect in OXPHOS efficiency and
229 a slight metabolic dependency on glycolysis (Fig. 3C and Supplementary Fig. 3A).

230 To dissect functional differences in the ETC complexes at the mitochondria between control and
231 mutant fibroblasts, we complemented our studies with the high-resolution Oxygraph-2k (O2k,
232 Oroboros Instruments, Austria) which measures OXPHOS within intact, permeabilized cells (Ye

233 and Hoppel, 2013). This method includes two protocols run in parallel (Hsiao and Hoppel, 2018;
234 Krahenbuhl et al., 1991; Ye and Hoppel, 2013) using a number of selective substrates and
235 inhibitors to measure the rates of oxygen consumption attributed to distinct ETC complexes. In
236 protocol 1, the activity of complexes I, II, and IV is sequentially assessed and measured. First,
237 intact cellular respiration (ICR) is determined to obtain a baseline rate prior to the addition of any
238 substrates. Consistent with the Seahorse analyzer, the DRP1 mutant fibroblasts showed
239 equivalent baseline OXPHOS to control fibroblasts (Fig. 3D). Then, substrates for Complex I (CI),
240 malate (M) and pyruvate (P), were added, but elicit no impact on the cellular respiration as these
241 substrates remain extracellular (Fig. 3E). To permeabilize the cell membrane, digitonin (Dig) was
242 added, resulting in diluted intracellular content and allowing M + P to enter the cell for oxidation,
243 which reveals the leak rate in the absence of ADP. In this assay, there was not a significant
244 increase in proton leak between control and mutant fibroblasts when substrate was not limited
245 (Fig. 3F). Based on our results from Seahorse where the major phenotype between the mutant
246 lines and the control fibroblasts was in the decreased coupling efficiency of the mitochondria, we
247 examined the functionality of each of the ETC complexes. Thus, adenosine diphosphate (ADP)
248 was added, to stimulate respiration of coupled mitochondria (also known as state 3)(Hsiao and
249 Hoppel, 2018; Ye and Hoppel, 2013), followed by addition of glutamate (G), another CI substrate,
250 and succinate (S), a complex II substrate. The addition of these compounds provides an
251 assessment of the coupled CI OXPHOS and the coupled CI + CII OXPHOS. While we found no
252 significant differences in the CI capacity (Fig. 3G), the DRP1 G32A fibroblasts showed a
253 significant decrease in the coupled CI/CII OXPHOS (Fig. 3H). We then assess the maximal
254 oxidative capacity, by adding the uncoupler, trifluoromethoxy carbonylcyanide phenylhydrazone
255 (FCCP), and saw a slight decrease, albeit not significant in the DRP1 G32A fibroblasts (Fig. 3I).
256 Next, the addition of rotenone (Rot), an inhibitor of CI, assesses the uncoupled CI and CII rates
257 individually. No significant differences were detected (Fig. 3J-K). To assess complex CIV Oxphos,
258 we added tetramethyl-p-phenylenediamine (TMPD) and ascorbate (AS), which donates electrons

259 to cytochrome c (cyt c), then a CIV inhibitor, azide, was added. No differences in CIV activity were
260 detected (Fig. 3L). Thus, our assessment of complexes I, II, and IV in the mutant G32A fibroblasts
261 revealed a potential deficiency in the linked CI/CII mitochondrial OXPHOS. This decrease in
262 linked CI/CII activity is likely due to the additive effect of combined rate since both CI and CII
263 trended down on their own. This decreased in CI and CII activity was not seen in the R403C
264 fibroblasts.

265 In protocol 2, we measured the OXPHOS for FAO and complex III (CIII). The ICR rate was first
266 assessed (Fig 3M). Followed by the addition of Malate (M) and palmitoylcarnitine (Pal), a long-
267 chain fatty acid derivative (Fig. 3N-O). We found that the ICR was significantly higher in the DRP1
268 R403C mutant fibroblasts (Fig. 3M-N) and significantly decreased in DRP1 G32A fibroblasts upon
269 addition of M and P (Fig. 3O). Upon permeabilization with Digitonin, ADP was then added to
270 assess the state 3 rate of Pal oxidation. No significant overall differences in the rate of FAO were
271 detected under these conditions (Fig. 3P). We followed by the addition of Rot to diminish any
272 non-mitochondrial oxidation, and duroquinol (DHQ), a CIII substrate, to assess the coupled CIII
273 rate (Fig. 3Q). Finally, the uncoupled CIII rate was evaluated via the addition of FCCP. There
274 were no differences in the coupled CIII activity or the uncoupled CIII oxidation. Collectively, our
275 results showed impaired coupled CI/CII activity in G32A but not R403C fibroblasts, and a potential
276 increase in FAO capacity in R403C mutants.

277 The upregulation of glycolysis with no accompanied increase in OXPHOS led us to interrogate a
278 potential impairment in pyruvate transport. Two proteins are essential for mitochondrial pyruvate
279 transport in humans, Mitochondrial Pyruvate Carrier 1 and 2 (MPC1 and MPC2) (Bricker et al.,
280 2012; Herzig et al., 2012). MPC1 and MPC2 associate to form an ~150-kilodalton complex in the
281 inner mitochondrial membrane. Real time quantitative PCR (RT-qPCR) gene expression analysis
282 showed a significant downregulation of *MPC2* expression in R403C cells and *MPC1* in both
283 patient lines (Supplementary Fig. 3B). These data suggest that the upregulation in glycolysis seen

284 in DRP1 mutant patient fibroblasts is accompanied by impaired pyruvate import into the
285 mitochondria. We examined the expression of MPC1 and MPC2, using Western blot, which
286 revealed a significant decrease in MPC2 expression in the R403C cells (Supplementary Fig. 3C)

287 The major contributor of the proton motive force of the ETC is the mitochondrial membrane
288 potential, which drives OXPHOS. Thus, changes in coupling efficiency can point to perturbation
289 of the mitochondrial membrane potential and the maintenance of key ion gradients. We
290 investigated this possibility using the fluorescent sensor Tetramethylrhodamine, ethyl ester
291 (TMRE). TMRE is a cell-permeant, cationic, red-orange fluorescent dye that is sequestered by
292 polarized mitochondria. We found that mitochondrial membrane potential as reported by TMRE
293 was significantly increased in patient fibroblasts (Fig. 4), indicative of hyperpolarization of the
294 mitochondria.

295 **DRP1 mutations alter mitochondrial cristae morphology**

296 Cristae topology readjustments participate in energy balance control (Eramo et al., 2020; Kondadi
297 et al., 2020). The hyperpolarization of the mitochondrial membrane detected in patient fibroblasts
298 lead us to assess the effects of DRP1 mutations on cristae morphology. We used a previously
299 optimized method to quantify and analyze cristae morphology changes from transmission electron
300 microscopy (TEM) (Eisner et al., 2017; Lam et al., 2021). In this method, cristae abundance is
301 calculated by manually quantifying the number of cristae per mitochondrion, and a score between
302 0 (worst) and 4 (best) is assigned based on the morphology: (0—no well-defined cristae, 1—no
303 cristae in more than ~75% of the mitochondrial area, 2—no cristae in approximately ~25% of
304 mitochondrial area, 3—many cristae (over 75% of area) but irregular, 4—many regular cristae)
305 (Supplementary Fig. 4A). TEM of patient fibroblasts confirmed the mitochondrial elongation
306 observed in SIM (Supplementary Fig. 4B-E) and revealed differences in the cristae structure (Fig.
307 5A). The quantification of cristae morphology demonstrated a reduced cristae score and
308 decreased cristae number relative to mitochondrial length in DRP1-deficient cells compared with

309 the control cells (Fig. 5B). These data link aberrant outer mitochondrial membrane fission caused
310 by DRP1 mutations to generalized cristae structural changes. The structure and respiratory
311 function of mitochondrial cristae are maintained by the mitochondrial contact sites and cristae
312 organizing system (MICOS) – a large complex of scaffolding and membrane shaping proteins
313 localized at the inner mitochondrial membrane. Given the reduced cristae score, we examined
314 expression of some key components of the MICOS complex. *MIC19, MIC25,* and *MIC60* are all
315 reduced in either one or both patient lines at the mRNA level; however, protein expression is not
316 significantly changed (Supplementary Fig. 4F). Thus, the structural abnormalities seen in patient
317 fibroblasts are not due to changes in the expression of MICOS proteins. Additional biochemical
318 assays are needed to assess the functionality of these proteins in the context of EMPF1.

319 **Patient fibroblasts display hyperfused peroxisomes**

320 In addition to catalyzing mitochondrial fission, DRP1 also participates in peroxisomal fission
321 (Kamerkar et al., 2018). While fission of peroxisomes has been demonstrated to be involved in
322 *de novo* peroxisomal biogenesis, the functional consequences of peroxisomal fission are not
323 completely understood. Previous reports using EMPF1 patient fibroblasts have not reported
324 elongation of peroxisomes, but DRP1 null cells have been reported to have hyperfused
325 peroxisomes (Kamerkar et al., 2018). To interrogate the effects of DRP1 mutations on peroxisome
326 morphology, we performed super-resolution microscopy. SIM revealed that both mutations in
327 DRP1 result in significant elongation of peroxisomes (Fig. 6A). Quantification of the peroxisome
328 structure shows an increase in volume, surface area, and length of peroxisomes (Fig. 6B),
329 demonstrating that DRP1 mutations found in patients with EMPF1 result in impaired peroxisome
330 fission.

331 Since peroxisomes and mitochondria are hubs for the regulation of fatty acid metabolism, we first
332 tested whether the dramatic changes in morphology would alter the expression of key genes
333 involved in fatty acid oxidation in patient fibroblasts. The expression of these genes have

334 previously been reported to increase in a DRP1 phosphomimetic mouse model (Valera-Alberni et
335 al., 2021). RT-qPCR analysis showed that the expression of carnitine palmitoyltransferase I,
336 *CPT1*, and acyl-coA dehydrogenase medium chain, *ACADM*, are significantly lower in patient
337 cells compared to control (Fig. 6C). CPT1 is associated with the outer mitochondrial membrane
338 and is responsible for catalyzing the transfer of the acyl group of acyl-CoA to L-carnitine. Fatty
339 acids are then able to move from the cytosol into the inner membrane space of the mitochondria
340 and the matrix, where fatty acid oxidation occurs. *ACADM* encodes for the medium-chain-acyl-
341 CoA dehydrogenase (MCAD) protein, which catalyzes the first step of mitochondrial fatty acid
342 beta-oxidation. Thus, the reduction in *CPT1* and *ACADM* expression may hinder the ability of the
343 mitochondria to carryout fatty acid oxidation.

344 To examine the ability of patient fibroblasts to perform fatty acid oxidation, we used the Seahorse
345 analyzer to quantify oxygen consumption rates of patient fibroblasts treated with either vehicle or
346 etomoxir, a CPT1 inhibitor. The cells were cultured with minimal glucose and glutamine and high
347 L-carnitine and palmitate to promote fatty acid oxidation over glycolysis or glutaminolysis. Control
348 fibroblasts treated with etomoxir, an inhibitor of CPT1, show a reduction in maximal respiration
349 following FCCP injection. In contrast, the G32A patient-derived cells show no change in OCR with
350 etomoxir treatment and the R403C patient-derived cells show an increase in maximal respiration
351 following FCCP injection (Fig. 6D-E). These data indicate that in contrast to the reliance of control
352 cells to long chain fatty acid oxidation under conditions of maximal respiration, both patient lines
353 have lost this dependency and adapted to the inhibition of long-chain fatty acid import into
354 mitochondria under these conditions. These data show that fibroblasts with DRP1 mutations
355 appear to have compensatory adaptations to alterations in long-chain fatty acid oxidation.

356 **Mitochondrial hyperfusion is rescued by MFN2 silencing**

357 The exact mechanisms by which the mitochondrial fusion machinery is positioned to sites of
358 fusion are not completely understood. However, fission and fusion events occur in rapid

359 succession (Liu et al., 2009) and fission and fusion machineries localize in close proximity at the
360 endoplasmic reticulum membrane contact sites (Abrisch et al., 2020). Given the intricate
361 relationship between these opposing dynamics, we examined the rates of fission and fusion in
362 live cells to determine if defects in fission may impact fusion rates. Our analysis in live cells
363 showed that in control cells the number of fission and fusion events per frame are very similar,
364 supporting the concept that these dynamic events are in equilibrium and constantly occurring in
365 tandem to one another under physiological conditions. By contrast, in patient cells, the reduced
366 number of fission events was accompanied by a significantly decreased number of fusion events
367 (Fig. 7A). Thus, defective fission leads to fewer fusion events contributing to decreased dynamic
368 mitochondrial network phenotype seen in patient cells.

369 The deleterious effects of fission deficiency have been shown to be restored by the concomitant
370 deletion of the mitochondrial fusion machinery (Chen H., et al., 2015). To further determine the
371 contribution of fusion to the mitochondrial network phenotype, we next tested whether deletion of
372 MFN2 would rescue the mitochondrial hyperfusion phenotype in patient fibroblasts. Indeed, MFN2
373 deletion restored all the parameters of mitochondrial morphology altered by DRP1 mutations (Fig.
374 7B), while the peroxisomal elongation was not completely restored (Supplementary Fig. 5).
375 Collectively these results show that the mitochondrial hyperfusion phenotype can be rescued by
376 modulating the levels of mitochondrial fusion.

377

378 **Discussion**

379 DRP1 is an essential gene for embryonic development (Ishihara et al., 2009; Wakabayashi et al.,
380 2009). RNAi based approaches in human cell culture models have been used to explore the
381 impact of DRP1 loss on mitochondrial fission and downstream processes such as apoptosis and
382 mitophagy (Kleele et al., 2021; Otera et al., 2016; Smirnova et al., 2001). Although loss of DRP1
383 results in mitochondrial hyperfusion, it's not fully understood how mutations in DRP1 can impact

384 cellular metabolic function, cristae structure, and/or peroxisomal function. The analysis of
385 organelle morphology in fibroblast lines derived from patients with EMPF1 that harbor one wild-
386 type copy of DRP1 and one missense copy of DRP1, demonstrate a dominant negative effect of
387 mutant DRP1 that results in stalling of the fission machinery that has a wide impact on cellular
388 function.

389 Mitochondrial fission is essential for cellular processes such as apoptosis, mitophagy, and
390 mitochondrial biogenesis. However, how mitochondrial fission helps maintain cristae structure
391 and/or cellular metabolism have not been thoroughly explored. Our studies revealed that while
392 DRP1 is recruited to the mitochondria in EMPF1 patient cell lines, the fission event is incomplete,
393 and thus, mitochondrial fission is paused. This stalling of mitochondrial fission results in dramatic
394 changes to cristae morphology, notably a decrease in cristae score and number, indicative of
395 immature and poorly formed cristae. Changes in redox signaling can lead to cysteine oxidation of
396 MIC60 (Li et al., 2021; Wasilewski and Chacinska, 2021), an inner mitochondrial membrane
397 protein responsible for cristae structure integrity. Thus, the lack of proper mitochondrial fission in
398 patient cells may disrupt redox signaling, which may in turn be responsible for the aberrant cristae
399 morphology detected in patient cells.

400 Detailed metabolic analysis of patient fibroblasts showed that these cells have decreased
401 coupling efficiency and upregulation of glycolysis, suggesting that the functional impact of stalled
402 fission is electron transport chain inefficiency. This inefficiency may be due to the changes in
403 cristae structure, since cristae structure is essential for F_0F_1–ATPase to function effectively (Afzal
404 et al., 2021; Cogliati et al., 2013; Davies et al., 2011; Wilkens et al., 2013). Previous studies
405 revealed that there are distinct fission signatures that are key determinants of the decision of
406 mitochondria to proliferate or degrade (Kleele et al., 2021). Peripheral fission events were shown
407 to be preceded by a decrease in membrane potential and proton motive force. We found that the
408 elongated mitochondria from patient fibroblasts have a hyperpolarized membrane potential, which

409 could result from inefficient function of the F_0F_1–ATPase. Under certain conditions, the F_0F_1–
410 ATPase can pump protons out of the mitochondrial matrix into the intermembrane space in a
411 reverse-mode action, causing ΔΨm hyperpolarization. Alternatively, hyperpolarization may be
412 due to complex I inhibition or VDAC (voltage-dependent anion channel) opening, which can cause
413 hyperpolarization independently of F_0F_1–ATPase reverse-mode action (Forkink et al., 2014). A
414 comprehensive analysis of the functionality of the ETC complexes would be needed to elucidate
415 the connection between fission stalling events and mitochondrial hyperpolarization. Upregulation
416 of glycolysis in these patient fibroblasts could result in subsequent glucose depletion locally within
417 the cells, which could in turn cause ΔΨm hyperpolarization. Carbon-tracing could help reveal
418 whether all of the products of glycolysis are efficiently shuttled into the TCA cycle or if
419 intermediates are lost in the process. Investigating the function of uncoupling proteins such as
420 UCP2 and UCP3 may elucidate whether the decreased efficiency is a byproduct or cause of
421 mitochondrial dysfunction, such as increased ΔΨm, in these cells. Our finding that cells with
422 DRP1 mutations have profound alterations in cristae morphology but apparent maintenance of
423 overall ATP production, raises the interesting possibility that DRP1 mutant cells have evolved
424 specialized mechanisms to cope with electron leakage and damaging reactive oxygen species. A
425 landmark study from Spinelli and collaborators demonstrated the ability of complex II to work in
426 reverse in some tissues with the intrinsic capacity to use fumarate as a terminal electron acceptor
427 (Spinelli et al., 2021). It is plausible that complex II reversal has evolved as a mechanism to
428 maintain mitochondrial function in cells with alterations in fission caused by DRP1 mutations.

429 The existence of two mechanistically and functionally distinct types of fission at the mitochondria
430 and the peroxisomes have not been clearly elucidated. In our study, we demonstrate that patient
431 fibroblasts with mutations in DRP1 also have elongated peroxisomal morphology. Previous
432 studies in mammalian cell culture revealed that peroxisome membrane elongation precedes
433 membrane constriction and final membrane fission (Delille et al., 2010; Schrader et al., 2016).

434 Whether peroxisomes have a specialized fusion machinery is still under debate. However, we
435 speculate that under particular metabolic conditions, peroxisomes, particularly those in contact
436 with mitochondria, may be able to fuse to respond to cellular metabolic needs. Elongation of the
437 peroxisomes in various human disorders has been associated with alterations in fatty acid
438 oxidation (Waterham et al., 2016). However, in these cells, peroxisomal function cannot be fully
439 dissociated from changes in mitochondrial morphology. Our results suggest that MFN2 silencing
440 could serve as a useful tool to discern the contribution of peroxisomal elongation independently
441 of the mitochondrial network. Our model (Fig. 7) suggests that the mechanistic and functional
442 connection between peroxisome remodeling and metabolic homeostasis could be dysregulated
443 in mitochondrial diseases such EMPF1. We propose that in this context, human diseases could
444 provide insight into the causal mechanisms underlying basic cellular processes, such as organelle
445 fission. The detailed elucidation of DRP1-centric mechanisms will reveal the connection between
446 organelle dynamics and cell fate. Several questions remain: Does stalling of mitochondrial fission
447 affect the association/dissociation of other proteins at the site of fission? Is peripheral fission also
448 inhibited in patient fibroblasts? If that is the case, what are the consequences for mitophagy and
449 mitochondrial DNA integrity? What are the effects of peroxisomal elongation on fatty acid
450 metabolism? How is cell division and mitochondrial segregation affected by DRP1 mutations?
451 How are cell fate transitions affected by DRP1 mutations? Answering these fundamental
452 questions would provide insight into the mechanisms of mitochondrial fission under the lens of
453 this rare disease caused by dysregulated mitochondrial and peroxisomal homeostasis and inform
454 the field on more rational and specific therapeutic targets for these devastating
455 neurodevelopmental disorders.

456

457 **STAR Methods**

458 **Cell Culture**

459 Human fibroblasts were thawed and plated directly in maintenance medium consisting of MEM
460 (Gibco #11095098) with 10% FBS (Sigma-Aldrich #F2442) and non-essential amino acids (Gibco
461 # 11-140-050). Cells were maintained at 37°C and 5% CO2 with media changes every other day.
462 Cells were passaged as needed using TrypLE (Thermo Fisher #12-064-013). For imaging
463 experiments, cells were re-plated onto #1.5 glass-bottom 35 mm dishes (Cellvis #D35C4-20-1.5-
464 N).

465 **Cell Treatments**

466 All treatments were added directly to fibroblasts in maintenance medium. The electron transport
467 chain decoupler CCCP (Sigma-Aldrich #C2759-250MG) was added to cells at a concentration of
468 1 μM. Cells were treated for 2 hours prior to fixation and imaging. All stock solutions were prepared
469 in DMSO.

470 **Plasmid Transfection**

471 Plasmid encoding mCherry-DRP1 (Addgene #49152) was transfected using FuGENE (Promega
472 #E2311) as described in the manufacturer protocol. Patient mutations were introduced to
473 plasmids using the In Fusion cloning kit (Takara Bio #638909) as described in the manufacturer
474 protocol. Cells were maintained until optimal transfection efficiency was reached before cells were
475 imaged.

476 **siRNA Transfection**

477 siRNA knockdown against MFN2 (Thermo Fisher #s19260) or negative control scrambled was
478 performed using Lipofectamine RNAiMAX tranfection reagent (Thermo Fisher # 13778150). Cells
479 were fixed and stained 48hrs after transfection.

480 **Immunofluorescence**

481 For immunofluorescence, cells were fixed with 4% paraformaldehyde for 20 min and
482 permeabilized in 1% Triton-X-100 for 10 min at room temperature. After blocking in 10% BSA,

483 cells were treated with primary and secondary antibodies using standard methods. Cells were
484 mounted in Fluoromount-G (Electron Microscopy Sciences #17984-25) prior to imaging. Primary
485 antibodies used include mouse anti-Mitochondria (Abcam #ab92824), rabbit anti-Tom20 (Cell
486 Signaling Technology #42406S), rabbit anti-DRP1 (Cell Signaling Technology #8570S), rabbit
487 anti-HSP60 (Cell Signaling Technologies # 12165S), mouse anti-PMP70 (Thermo Fisher # MA5-
488 31368), and rabbit anti-pDRP1 S616 (Cell Signaling Technology #3455S). Secondary antibodies
489 used include donkey anti-mouse Alexa Fluor-488 (Thermo Fisher Scientific #A21202), donkey
490 anti-rabbit Alexa Fluor-488 (Thermo Fisher Scientific #A21206), and donkey anti-mouse Alexa
491 Fluor-546 (Thermo Fisher Scientific #A10036), and donkey anti-rabbit Alexa Fluor-546 (Thermo
492 Fisher Scientific #A10040).

493 **Western Blot**

494 Gel samples were prepared by mixing cell lysates with LDS sample buffer (Life Technologies,
495 #NP0007) and 2-Mercaptoethanol (BioRad #1610710) and boiled at 95°C for 5 minutes. Samples
496 were resolved on 4-20% Mini-PROTEAN TGX precast gels (BioRad #4561096) and transferred
497 onto PVDF membrane (BioRad #1620177). Antibodies used for Western blotting are as follows:
498 rabbit anti-DRP-1 (Cell Signaling Technologies #8570S), rabbit anti-pDRP-1 S616 (Cell Signaling
499 Technologies #3455S), rabbit anti-OPA1 (Cell Signaling Technologies #67589S), mouse anti-
500 MFN1 (Abcam #ab57602, mouse anti-MFN2 (Abcam #ab56889), rabbit anti-MFF (Proteintech
501 #17090-1-AP), rabbit anti-MiD49 (Proteintech #16413-1-AP), rabbit anti-MiD51 (Proteintech
502 #20164-1-AP), and rabbit anti-FIS1 (Proteintech #10956-1-AP), and mouse anti-HSP70
503 (Invitrogen #MA3-006).

504 **Seahorse XF Analysis**

505 Fibroblasts were plated onto Seahorse XF96 V3 PS cell culture microplates 2 days before the
506 assay at 50,000 cells per well. One hour prior to the assay, media was switched to XF DMEM
507 media containing 1 mM pyruvate, 2 mM glutamine, and 10 mM glucose. For the Seahorse XF

508 Mito Stress Test, oxygen consumption rate (OCR) was measured sequentially after addition of
509 1.0 μM oligomycin, 0.5 μM FCCP, and 0.5 μM rotenone plus Antimycin A. Protein leak and
510 coupling efficiency were calculated using OCR. For the Seahorse XF Glycolytic Rate Assay, basal
511 glycolytic rate was measured by extracellular acidification, and compensatory glycolysis was
512 measured after addition of 0.5 μM rotenone plus antimycin A. Treatment with 50 mM 2-DG was
513 used as a negative control. For the Seahorse XF Fuel Flex Test, glutamine dependency was
514 measured by sequential addition of 3.0 μM BPTES followed by 4.0 μM Etomoxir plus 2.0 μM
515 UK5099. Fatty acid dependency was measured by sequential addition of 4.0 μM Etomoxir
516 followed by 3.0 μM BPTES plus 2.0 μM UK5099. Glucose dependency was measured by
517 sequential addition of 2.0 μM UK5099 followed by 3.0 μM BPTES plus 4.0 μM Etomoxir. For the
518 Seahorse XF Long Chain Fatty Acid Oxidation Stress Test, 24 hours prior to assay cells were
519 switched to base media containing 0.5 mM glucose, 1.0 mM glutamine, 0.5 mM XF L-carnitine,
520 and 1.0 % fetal bovine serum. One hour prior to the assay, media was switched to XF DMEM
521 media containing 2 mM glucose, 0.5 mM L-Carnitine, and Palmitate-BSA. Oxygen consumption
522 rate (OCR) was measured sequentially after addition of 4.0 μM etomoxir, 1.5 μM oligomycin, 2.0
523 μM FCCP, and 0.5 μM rotenone plus Antimycin A.

524 **O2K Analysis**

525 Oxygen consumption was measured with an O2K system (OROBOROS) using Protocols 1 and
526 2 described in Ye and Hoppel, 2013. Briefly, 2 ml of cell suspension (600,000 cells/ml) in Mir05
527 buffer was added to each chamber. Initial substrates were added (malate and pyruvate in protocol
528 1 and malate and palmitoylcarnitine in protocol 2) followed by addition of digitonin in increments
529 (2ug/ml) to permeabilize the cell membranes. The final concentration of substrates and inhibitors
530 was composed of malate (2 mM), pyruvate (2.5 mM), adenosine diphosphate (ADP, 2.5 mM),
531 glutamate (10 mM), succinate (10 mM), palmitoylcarnitine (10 μM), duroquinol (0.5 mM),
532 etramethyl-p-phenylenediamine (TMPD, 0.5 μM), ascorbate (2 mM), carbonylcyanide-p-

533 trifluoromethoxy- phenylhydrazone (FCCP, 0.5-μM increment), rotenone (75 nM), antimycin A
534 (125 nM), and sodium azide (200 mM). For Protocol 1, the non-mitochondrial (AA-insensitive) rate
535 was subtracted. For Protocol 2, the Rot-insensitive rate was subtracted. For DHQ, the AA was
536 subtracted.

537 **RNA Extraction and cDNA Synthesis**

538 Cells were washed with PBS and scraped into 1000μl Trizol reagent. 200μl of chloroform was
539 added and the samples were incubated at room temperature for 5 minutes. The samples were
540 spun down at 12,000 g and the aqueous phase was collected. 500μl of isopropanol was added
541 to precipitate RNA and the sample was incubated for 25 minutes at room temperature, followed
542 by centrifugation at 12,000 g for 10 min at 4°C. The RNA pellet was washed with 75% ethanol,
543 semi-dried, and resuspended in 30μl of DEPC water. After quantification and adjusting the volume
544 of all the samples to 1μg/μl, the samples were treated with DNAse (New England Biolabs, #
545 M0303). 10μl of this volume was used to generate cDNA using the manufacturer's protocol
546 (Thermo Fisher, #4368814).

547 **Quantitative RT PCR (RT-qPCR)**

548 1ug of cDNA sample was used to run RT-qPCR for the primers mentioned in the table.
549 QuantStudio 3 Real-Time PCR machine, SYBR green master mix (Thermo Fisher, #4364346),
550 and manufacturer instructions were used to set up the assay.

551 **Image Acquisition**

552 Super-resolution images were acquired using a Nikon SIM microscope equipped with a 1.49 NA
553 100x Oil objective an Andor DU-897 EMCCD camera. Live-imaging experiments were acquired
554 on a Nikon Eclipse Ti-E spinning disk confocal microscope equipped with a 1.40 NA 60X Oil
555 objective and an Andor DU-897 EMCCD camera. Image processing and quantification was
556 performed using Fiji.

557 **Sample Preparation for Transmission Electron Microscope (TEM) Analysis**

558 Human fibroblasts were immediately washed in ice-cold saline. Samples were processed as
559 described by (Lam et. al., 2021, Pereira et al., 2017). Cells were fixed in 2.5% glutaraldehyde in
560 sodium cacodylate buffer for 1 hour at 37 °C, embedded in 2% agarose, postfixed in buffered 1%
561 osmium tetroxide, stained in 2% uranyl acetate, and dehydrated with an ethanol graded series.
562 After embedding in EMbed-812 resin, 80 nm sections were cut on an ultramicrotome and stained
563 with 2% uranyl acetate and lead citrate. Images were acquired on a JEOL JEM-1230
564 Transmission Electron Microscope, operating at 120 kV. Random images of human fibroblasts
565 were obtained.

566 **TEM Analysis**

567 Measurements of mitochondrial area, circularity, and length were performed using the multi-
568 measure region of interest (ROI) tool in ImageJ (Lam et. al., 2021, Parra et al., 2014). To measure
569 cristae morphology, we used ROIs in ImageJ to determine the cristae area, circulatory index,
570 number, volume, and cristae score. The NIH ImageJ software was used to manually trace and
571 analyze all mitochondria or cristae using the freehand told in the ImageJ application (Lam et. al.,
572 2021, Parra et al., 2014). To assign a mitochondrion a cristae score, cristae abundance and form
573 were evaluated. A score between 0 and 4 (0 – no sharply defined crista, 1 – greater than 50% of
574 mitochondrial area without cristae, 2 – greater than 25% of mitochondrial area without cristae, 3
575 – many cristae but irregular, 4 – many regular cristae) was assigned (Eisner et al., 2017).

576 **Serial Block Facing-Scanning Electron Microscopy (SBF-SEM) Processing**

577 Human fibroblasts were fixed in 2% glutaraldehyde in 0.1 M cacodylate buffer and processed
578 using a heavy metal protocol adapted from a previously published protocol (Courson et al., 2021;
579 Mustafi et al., 2014). Human fibroblasts were immersed in 3% potassium ferrocyanide and 2%
580 osmium tetroxide (1 hour at 4 °C), followed by filtered 0.1% thiocarbohydrazide (20 min), 2%
581 osmium tetroxide (30 min), and left overnight in 1% uranyl acetate at 4 °C (several de-ionized

582 H2O washes were performed between each step). The next day samples were immersed in a
583 0.6% lead aspartate solution (30 min at 60 °C and dehydrated in graded acetone (as described
584 for TEM). Human fibroblasts were impregnated with epoxy Taab 812 hard resin, embedded in
585 fresh resin, and polymerized at 60 °C for 36–48 hours. After polymerization, the block was
586 sectioned for TEM to identify the area of interest, then trimmed to 0.5 mm × 0.5 mm and glued to
587 an aluminum pin. The pin was placed into an FEI/Thermo Scientific Volumescope 2 scanning
588 electron microscope (SEM). The scope is a state-of-the-art SBF imaging system. For 3D EM
589 reconstruction, thin (0.09 μm) serial sections, 300 to 400 per block, were obtained from the blocks
590 that were processed for conventional TEM. Serial sections were collected onto formvar coated
591 slot grids (Pella, Redding CA), stained, and imaged, as described above. The segmentation of
592 SBF-SEM reconstructions was performed by manually tracing structural features through
593 sequential slices of the micrograph block. Images were collected from 30–50 serial sections,
594 which were then stacked, aligned, and visualized using Amira to make videos and quantify
595 volumetric structures.

596 **Mitochondrial Event Localizer (MEL)**

597 The MEL algorithm processes a fluorescence microscopy time-lapse sequence of z-stack images
598 of Mitotracker- labeled mitochondria and produces event counts per frame and 3D locations
599 indicating where mitochondrial events are likely to have occurred at each time step(Theart et al.,
600 2020). These locations can subsequently be superimposed on the z-stacks to indicate the
601 different mitochondrial events. The algorithm has been organized into two consecutive steps,
602 namely the image pre-processing step which normalizes and prepares the time-lapse frames, and
603 the automatic image analysis step which calculates the location of the mitochondrial events based
604 on the normalized frames. MEL also allows each event to be subsequently validated and removed
605 from the visualization and event counts. The code is available for download:
606 https://github.com/rensutheart/MEL-Fiji-Plugin.

607 **Statistical Analysis**

608 All experiments were performed with a minimum of 3 biological replicates. Statistical significance
609 was determined by one-way or repeated measures one-way analysis of variance (ANOVA) as
610 appropriate for each experiment. significance was assessed using Fisher's protected least
611 significance difference test. GraphPad PRISM v8.1.2and Statplus software package were used
612 GraphPad Prism was used for all statistical analysis (SAS Institute: Cary, NC, USA). and data
613 visualization. Error bars in all bar graphs represent standard error of the mean unless otherwise
614 noted in the figure. No outliers were removed from the analyses. Quantification of mitochondrial
615 morphology was performed in NIS-Elements (Nikon); briefly, we segmented mitochondria in 3D
616 and performed skeletonization of the resulting 3D mask. Skeleton major axis length, volume, and
617 surface area measurements were exported into Excel. For all statistical analyses, a significant
618 difference was accepted when $P < 0.05$.

619

620 **Acknowledgements**

621 We would like to thank the patients and families for permission to publish this work. We thank Dr.
622 Eric Payne and Dr. Suzanne Hoppins for providing the patient-derived fibroblast lines used in this
623 paper. We would also like to thank Dr. Evan Krystofiak for providing EM expertise, and Dr.
624 Matthew Tyska, Dr. Uri Manor, and Dr. Kari Seedle, for providing advice and expertise with high-
625 resolution microscopy. This work was supported by 1R35 GM128915-01NIGMS (VG),
626 1RF1MH123971-01 (VG); the Precision Medicine and Mental Health Initiative sponsored by the
627 Vanderbilt Brain Institute (VG), 1R21CA227483-01A1NCI (VG), F99NS125829 (GLR), HHMI
628 Gilliam (GLR), and CBMS T32 (GLR). All SIM and spinning disk confocal microscopy imaging
629 and image analysis were performed in part through the use of the Vanderbilt Cell Imaging Shared
630 Resource, which is supported by NIH grants 1S10OD012324-01 and 1S10OD021630-01. The
631 authors declare no competing financial interests.

632

633 **Author Contributions**

634 G. Robertson and V. Gama conceived the study, designed experiments, interpreted data, and
635 wrote the manuscript. V. Gama supervised the research. G. Robertson designed and carried out
636 all the cell biology experiments, with technical assistance from M. Patel and S. Riffle. J. Mears
637 and M. Stoll performed the O2K experiments and provided technical feedback and insight into the
638 conception and execution of study. A. Marshall, H. Beasley, Z. Vue, J. Shao, and E. Garza Lopez
639 performed the TEM, 3D EM and sbf-SEM experiments, quantification, and analysis, with the
640 supervision of A. Hinton. S. de Wet, R. P. Theart, and Ben Loos, applied the MEL algorithm to
641 the mitochondrial imaging data to calculate fission and fusion events. All authors edited the
642 document.

643 **Figure Legends**

644 **Figure 1. DRP1 patient-derived fibroblasts have elongated mitochondrial morphology.** (A)
645 Structural and schematic representation of DRP1 with mutations highlighted in red. (B)
646 Representative images of mitochondrial morphology in patient-derived fibroblasts using
647 structured illumination microscopy (n=3, 7 cells per replicate). (C) Quantification of mitochondrial
648 volume, surface area, and major axis length. Analyzed using one-way ANOVA followed by
649 Dunnett's multiple comparison test. (D) Representative sbf-SEM 3D reconstructed images. Each
650 mitochondrion is colored a unique color. (E) Quantification of sbf-SEM for 3D mitochondrial length,
651 volume, and complexity index. Analyzed using one-way ANOVA followed by Dunnett's multiple
652 comparison test. (F) Representative images of mitochondrial morphology in control fibroblasts
653 transfected with either $DRP1^{WT}$-mCherry, $DRP1^{G32A}$-mCherry, or $DRP1^{R403C}$-mCherry using
654 structured illumination microscopy (n=3, 7 cells per replicate). (G) Quantification of mitochondrial
655 volume, surface area, and major axis length. Analyzed using one-way ANOVA followed by
656 Dunnett's multiple comparison test.

657 **Figure 2. Mutant G32A and R403C DRP1 are recruited to mitochondria.** (A) Western blot of
658 total protein lysate isolated from patient fibroblasts and probed for mitochondrial fusion proteins.
659 Representative image of three independent biological replicates. Band density is normalized to
660 loading control (HSP70) and relative to control cells. (B) Western blot of total protein lysate
661 isolated from patient fibroblasts and probed for mitochondrial fission proteins. Band density is
662 normalized to loading control (HSP70) and relative to control cells. Representative image of three
663 independent biological replicates. (C) Representative images of mitochondrial and DRP1 in
664 patient-derived fibroblasts using structured illumination microscopy (n=3, 7 cells per replicate).
665 Top image is a zoom of white box from bottom image. (D) Quantification of DRP1 puncta that
666 overlap with mitochondria and volume of DRP1 puncta. Analyzed using one-way ANOVA followed
667 by Dunnett's multiple comparison test. (E) Representative images of mitochondrial morphology in
668 patient-derived fibroblasts treated with either DMSO or CCCP for 1 hours using structured
669 illumination microscopy (n=3, 7 cells per replicate). (F) Quantification of mitochondrial volume,
670 surface area, and major axis length. Analyzed using one-way ANOVA followed by Dunnett's
671 multiple comparison test.

672 **Figure 3. Mitochondrial defects lead to inefficient coupling of the electron transport chain**
673 **and higher glycolytic rate.** (A) Oxygen consumption rate and extracellular acidification rate in
674 patient fibroblasts as measured using Seahorse Mitochondrial stress test (n=3, 20 wells per
675 replicate). Oligomycin applied at 20 minutes, FCCP applied at 40 minutes, and
676 rotenone/Antimycin A applied at 60 minutes. Analyzed using two-way ANOVA followed by Šídák's
677 multiple comparisons test. (B) Proton leak and coupling efficiency calculated using oxygen
678 consumption rate. (C) Basal glycolysis of patient fibroblasts measure using Seahorse Glycolytic
679 Rate Assay. Compensatory glycolysis measured following application of rotenone/Antimycin A.
680 (D-L) O_2 consumption rate of intact cells followed by isolated complex O_2 consumption using
681 protocol 1. Analyzed using one-way ANOVA followed by Dunnett's multiple comparison test. (M-

682 R) O_2 consumption rate of intact cells followed by isolated complex O_2 consumption using protocol
683 2. Analyzed using one-way ANOVA followed by Dunnett's multiple comparison test.

684 **Figure 4. DRP1 patient fibroblasts have more hyperpolarized mitochondrial membrane**
685 **potential.** (A) Representative live-cell imaging of patient-derived fibroblasts treated with 500nM
686 TMRE for 10 minutes. Cells were imaged every 15 seconds for 15 minutes using spinning disk
687 confocal (n=3, 7 cells per replicate). Scale bar: 5 µm.

688 **Figure 5. Cristae morphology is altered in patient cells.** (A) Transmission electron microscopy
689 of patient fibroblasts. 3 representative images per line shown. (B) Quantification of cristae from
690 TEM images for cristae score and cristae number relative to mitochondrial length. Analyzed using
691 one-way ANOVA followed by Dunnett's multiple comparison test.

692 **Figure 6. Patient fibroblasts have elongated peroxisomes.** (A) Representative images of
693 peroxisomal morphology in patient-derived fibroblasts using structured illumination microscopy
694 (n=3, 7 cells per replicate). (B) Quantification of peroxisomal volume, surface area, and major
695 axis length. Analyzed using one-way ANOVA followed by Dunnett's multiple comparison test. (C)
696 qRT-PCR analysis of gene expression in fibroblasts relative to control and normalized to two
697 housekeeping genes (*GPI* and *GAPDH)*. Quantifications are shown for three independent
698 biological replicates. (D) Oxygen consumption rate in patient fibroblasts as measured using
699 Seahorse Analyzer XFe96 (n=3, 20 wells per replicate). Etomoxir applied after 20 minutes,
700 oligomycin applied at 40 minutes, FCCP applied at 60 minutes, and rotenone/Antimycin A applied
701 at 80 minutes. Analyzed using two-way ANOVA followed by Šídák's multiple comparisons test.
702 (E) OCR at maximal respiration after FCCP treatment.

703 **Figure 7: Current model of the cellular responses to EMPF1 associated DRP1 mutations.**
704 (A) Representative images of mitochondrial dynamics in patient-derived fibroblasts treated with
705 Mitotracker Green with fission events marked in green and fusion events marked in red (7 cells

706 per replicate). (B) Quantification of mitochondrial dynamics using MEL. Analyzed using one-way
707 ANOVA followed by Dunnett's multiple comparison test. (C) Representative images of
708 mitochondrial and peroxisomal morphology in patient-derived fibroblasts treated with either siRNA
709 against MFN2 or scrambled using structured illumination microscopy (n=3, 7 cells per replicate).
710 (D) Quantification of mitochondrial volume, surface area, and major axis length. Analyzed using
711 one-way ANOVA followed by Dunnett's multiple comparison test. (E) Summary schematic:
712 EMPF1- associated mutations do not appear to alter the capacity of DRP1 to be recruited to points
713 of fission, but rather cause stalling of the fission events. Pausing peroxisomal and mitochondrial
714 fission results in alterations of cristae structure, changes in mitochondrial membrane potential,
715 decreased mitochondrial coupling efficiency, delayed cell death response, and overall metabolic
716 adaptations.

References

Afzal N, Lederer WJ, Jafri MS, Mannella CA. 2021. Effect of crista morphology on mitochondrial ATP output: A computational study. *Current Research in Physiology* **4**:163–176. doi:10.1016/J.CRPHYS.2021.03.005

Alexander C, Votruba M, Pesch UEA, Thiselton DL, Mayer S, Moore A, Rodriguez M, Kellner U, Leo-Kottler B, Auburger G, Bhattacharya SS, Wissinger B. 2000. OPA1, encoding a dynamin-related GTPase, is mutated in autosomal dominant optic atrophy linked to chromosome 3q28. *Nature Genetics 2000 26:2* **26**:211–215. doi:10.1038/79944

Bayraktar EC, Baudrier L, Özerdem C, Lewis CA, Chan SH, Kunchok T, Abu-Remaileh M, Cangelosi AL, Sabatini DM, Birsoy K, Chen WW. 2019. MITO-Tag Mice enable rapid isolation and multimodal profiling of mitochondria from specific cell types in vivo. *Proc Natl Acad Sci U S A* **116**:303–312. doi:10.1073/pnas.1816656115

Bricker DK, Taylor EB, Schell JC, Orsak T, Boutron A, Chen YC, Cox JE, Cardon CM, Van Vranken JG, Dephoure N, Redin C, Boudina S, Gygi SP, Brivet M, Thummel CS, Rutter J. 2012. A mitochondrial pyruvate carrier required for pyruvate uptake in yeast, Drosophila, and humans. *Science* **337**:96–100. doi:10.1126/SCIENCE.1218099

Chakrabarti R, Ji WK, Stan R V., Sanz J de J, Ryan TA, Higgs HN. 2018. INF2-mediated actin polymerization at the ER stimulates mitochondrial calcium uptake, inner membrane constriction, and division. *J Cell Biol* **217**:251–268. doi:10.1083/JCB.201709111

Chandel NS. 2021. Lipid Metabolism. *Cold Spring Harb Perspect Biol* **13**. doi:10.1101/CSHPERSPECT.A040576

Chang C, Blackstone C. 2007. Drp1 phosphorylation and mitochondrial regulation. *EMBO Rep* **8**:1088–1089. doi:10.1038/sj.embor.7401118

Chao YH, Robak LA, Xia F, Koenig MK, Adesina A, Bacino CA, Scaglia F, Bellen HJ, Wangler MF. 2016. Missense variants in the middle domain of DNM1L in cases of infantile encephalopathy alter peroxisomes and mitochondria when assayed in Drosophila. *Human Molecular Genetics* **25**:1846–1856. doi:10.1093/HMG/DDW059

Chen H, Detmer SA, Ewald AJ, Griffin EE, Fraser SE, Chan DC. 2003. Mitofusins Mfn1 and Mfn2 coordinately regulate mitochondrial fusion and are essential for embryonic development. *Journal of Cell Biology* **160**:189–200. doi:10.1083/JCB.200211046

Cogliati S, Frezza C, Soriano ME, Varanita T, Quintana-Cabrera R, Corrado M, Cipolat S, Costa V, Casarin A, Gomes LC, Perales-Clemente E, Salviati L, Fernandez-Silva P, Enriquez JA, Scorrano L. 2013. Mitochondrial Cristae Shape Determines Respiratory Chain Supercomplexes Assembly and Respiratory Efficiency. *Cell* **155**:160–171. doi:10.1016/J.CELL.2013.08.032

Csordás G, Renken C, Várnai P, Walter L, Weaver D, Buttle KF, Balla T, Mannella CA, Hajnóczky G. 2006. Structural and functional features and significance of the physical

linkage between ER and mitochondria. *Journal of Cell Biology* **174**:915–921. doi:10.1083/jcb.200604016

Davies KM, Strauss M, Daum B, Kief JH, Osiewacz HD, Rycovska A, Zickermann V, Kühlbrandt W. 2011. Macromolecular organization of ATP synthase and complex I in whole mitochondria. *Proc Natl Acad Sci U S A* **108**:14121–14126. doi:10.1073/PNAS.1103621108/-/DCSUPPLEMENTAL

Delettre C, Lenaers G, Griffoin JM, Gigarel N, Lorenzo C, Belenguer P, Pelloquin L, Grosgeorge J, Turc-Carel C, Perret E, Astarie-Dequeker C, Lasquellec L, Arnaud B, Ducommun B, Kaplan J, Hamel CP. 2000. Nuclear gene OPA1, encoding a mitochondrial dynamin-related protein, is mutated in dominant optic atrophy. *Nature Genetics 2000 26:2* **26**:207–210. doi:10.1038/79936

Delille HK, Agricola B, Guimaraes SC, Borta H, Lüers GH, Fransen M, Schrader M. 2010. Pex11pbeta-mediated growth and division of mammalian peroxisomes follows a maturation pathway. *J Cell Sci* **123**:2750–2762. doi:10.1242/JCS.062109

Ding L, Sun W, Balaz M, He A, Klug M, Wieland S, Caiazzo R, Raverdy V, Pattou F, Lefebvre P, Lodhi IJ, Staels B, Heim M, Wolfrum C. 2021. Peroxisomal β-oxidation acts as a sensor for intracellular fatty acids and regulates lipolysis. *Nat Metab* **3**:1648–1661. doi:10.1038/S42255-021-00489-2

Dorn GW. 2015. Mitochondrial dynamism and heart disease: changing shape and shaping change. *EMBO Molecular Medicine* **7**:865–877. doi:10.15252/emmm.201404575

Eisner V, Cupo RR, Gao E, Csordás G, Slovinsky WS, Paillard M, Cheng L, Ibetti J, Chen SRW, Chuprun JK, Hoek JB, Koch WJ, Hajnóczky G. 2017. Mitochondrial fusion dynamics is robust in the heart and depends on calcium oscillations and contractile activity. *Proc Natl Acad Sci U S A* **114**:E859–E868. doi:10.1073/PNAS.1617288114/-/DCSUPPLEMENTAL

Eramo MJ, Lisnyak V, Formosa LE, Ryan MT. 2020. The “mitochondrial contact site and cristae organising system” (MICOS) in health and human disease. *J Biochem* **167**:243–255. doi:10.1093/JB/MVZ111

Fahrner JA, Liu R, Perry MS, Klein J, Chan DC. 2016. A novel de novo dominant negative mutation in DNM1L impairs mitochondrial fission and presents as childhood epileptic encephalopathy. *Am J Med Genet A* **170**:2002–2011. doi:10.1002/AJMG.A.37721

Faitg J, Lacefield C, Davey T, White K, Laws R, Kosmidis S, Reeve AK, Kandel ER, Vincent AE, Picard M. 2021. 3D neuronal mitochondrial morphology in axons, dendrites, and somata of the aging mouse hippocampus. *Cell Reports* **36**. doi:10.1016/J.CELREP.2021.109509/ATTACHMENT/28BF2465-59D0-4B68-BCDD-D3F180754B5F/MMC1.PDF

Fan J, Li X, Issop L, Culty M, Papadopoulos V. 2016. ACBD2/ECI2-Mediated Peroxisome-Mitochondria Interactions in Leydig Cell Steroid Biosynthesis. *Mol Endocrinol* **30**:763–782. doi:10.1210/ME.2016-1008

Ferreira AR, Marques M, Ramos B, Kagan JC, Ribeiro D. 2021. Emerging roles of peroxisomes in viral infections. *Trends Cell Biol*. doi:10.1016/J.TCB.2021.09.010

797 Fonseca TB, Sánchez-Guerrero Á, Milosevic I, Raimundo N. 2019. Mitochondrial fission
798 requires DRP1 but not dynamins. *Nature*. doi:10.1038/s41586-019-1296-y

799 Forkink M, Manjeri GR, Liemburg-Apers DC, Nibbeling E, Blanchard M, Wojtala A, Smeitink
800 JAM, Wieckowski MR, Willems PHGM, Koopman WJH. 2014. Mitochondrial
801 hyperpolarization during chronic complex I inhibition is sustained by low activity of
802 complex II, III, IV and V. *Biochimica et Biophysica Acta (BBA) - Bioenergetics*
803 **1837**:1247–1256. doi:10.1016/J.BBABIO.2014.04.008

804 Fransen M, Lismont C, Walton P. 2017. The Peroxisome-Mitochondria Connection: How and
805 Why? *Int J Mol Sci* **18**. doi:10.3390/IJMS18061126

806 Friedman JR, Lackner LL, West M, DiBenedetto JR, Nunnari J, Voeltz GK. 2011. ER tubules
807 mark sites of mitochondrial division. *Science (1979)* **334**:358–362.
808 doi:10.1126/SCIENCE.1207385/SUPPL_FILE/FRIEDMAN.SOM.REV1.PDF

809 Fröhlich C, Grabiger S, Schwefel D, Faelber K, Rosenbaum E, Mears J, Rocks O, Daumke
810 O. 2013. Structural insights into oligomerization and mitochondrial remodelling of
811 dynamin 1-like protein. *EMBO J* **32**:1280–1292. doi:10.1038/EMBOJ.2013.74

812 Gandre-Babbe S, Van Der Bliek AM. 2008. The novel tail-anchored membrane protein Mff
813 controls mitochondrial and peroxisomal fission in mammalian cells. *Molecular Biology*
814 *of the Cell* **19**:2402–2412. doi:10.1091/MBC.E07-12-
815 1287/ASSET/IMAGES/LARGE/ZMK0060885640008.JPEG

816 Garza-Lopez E, Vue Z, Katti P, Neikirk K, Biete M, Lam J, Beasley HK, Marshall AG, Rodman
817 TA, Christensen TA, Salisbury JL, Vang L, Mungai M, AshShareef S, Murray SA, Shao
818 J, Streeter J, Glancy B, Pereira RO, Dale Abel E, Hinton A, Lopez G. 2021. Protocols
819 for Generating Surfaces and Measuring 3D Organelle Morphology Using Amira. *Cells*
820 *2022, Vol 11, Page 65* **11**:65. doi:10.3390/CELLS11010065

821 Hatch AL, Gurel PS, Higgs HN. 2014. Novel roles for actin in mitochondrial fission. *J Cell Sci*
822 **127**:4549–4560. doi:10.1242/JCS.153791

823 Hatch AL, Ji WK, Merrill RA, Strack S, Higgs HN. 2016. Actin filaments as dynamic reservoirs
824 for Drp1 recruitment. *Mol Biol Cell* **27**:3109–3121. doi:10.1091/MBC.E16-03-0193

825 Herzig S, Raemy E, Montessuit S, Veuthey JL, Zamboni N, Westermann B, Kunji ERS,
826 Martinou JC. 2012. Identification and functional expression of the mitochondrial
827 pyruvate carrier. *Science* **337**:93–96. doi:10.1126/SCIENCE.1218530

828 Hsiao CP, Hoppel C. 2018. Analyzing mitochondrial function in human peripheral blood
829 mononuclear cells. *Anal Biochem* **549**:12–20. doi:10.1016/J.AB.2018.03.003

830 Ishihara N, Nomura M, Jofuku A, Kato H, Suzuki SO, Masuda K, Otera H, Nakanishi Y,
831 Nonaka I, Goto YI, Taguchi N, Morinaga H, Maeda M, Takayanagi R, Yokota S, Mihara
832 K. 2009. Mitochondrial fission factor Drp1 is essential for embryonic development and
833 synapse formation in mice. *Nature Cell Biology* **11**:958–966. doi:10.1038/ncb1907

834 Itoyama A, Michiyuki S, Honsho M, Yamamoto T, Moser A, Yoshida Y, Fujiki Y. 2013. Mff
835 functions with Pex11pβ and DLP1 in peroxisomal fission. *Biology Open* **2**:998.
836 doi:10.1242/BIO.20135298

Iwata R, Casimir P, Vanderhaeghen P. 2020. Mitochondrial dynamics in postmitotic cells regulate neurogenesis. *Science (1979)* **369**:858–862. doi:10.1126/science.aba9760

Ji WK, Chakrabarti R, Fan X, Schoenfeld L, Strack S, Higgs HN. 2017. Receptor-mediated Drp1 oligomerization on endoplasmic reticulum. *J Cell Biol* **216**:4123–4139. doi:10.1083/JCB.201610057

Ji WK, Hatch AL, Merrill RA, Strack S, Higgs HN. 2015. Actin filaments target the oligomeric maturation of the dynamin GTPase Drp1 to mitochondrial fission sites. *Elife* **4**. doi:10.7554/eLife.11553

Kamerkar SC, Kraus F, Sharpe AJ, Pucadyil TJ, Ryan MT. 2018. Dynamin-related protein 1 has membrane constricting and severing abilities sufficient for mitochondrial and peroxisomal fission. *Nature Communications* **9**:1–15. doi:10.1038/s41467-018-07543-w

Keller N, Paketci C, Edem P, Thiele H, Yis U, Wirth B, Karakaya M. 2021. De novo DNM1L variant presenting with severe muscular atrophy, dystonia and sensory neuropathy. *Eur J Med Genet* **64**. doi:10.1016/J.EJMG.2020.104134

Khacho M, Clark A, Svoboda DS, Azzi J, MacLaurin JG, Meghaizel C, Sesaki H, Lagace DC, Germain M, Harper ME, Park DS, Slack RS. 2016. Mitochondrial Dynamics Impacts Stem Cell Identity and Fate Decisions by Regulating a Nuclear Transcriptional Program. *Cell Stem Cell* **19**:232–247. doi:10.1016/j.stem.2016.04.015

King WT, Axelrod CL, Zunica ERM, Noland RC, Davuluri G, Fujioka H, Tandler B, Pergola K, Hermann GE, Rogers RC, López-Domènech S, Dantas WS, Stadler K, Hoppel CL, Kirwan JP. 2021. Dynamin-related protein 1 regulates substrate oxidation in skeletal muscle by stabilizing cellular and mitochondrial calcium dynamics. *Journal of Biological Chemistry* **297**:101196. doi:10.1016/J.JBC.2021.101196

Kleele T, Rey T, Winter J, Zaganelli S, Mahecic D, Perreten Lambert H, Ruberto FP, Nemir M, Wai T, Pedrazzini T, Manley S. 2021. Distinct fission signatures predict mitochondrial degradation or biogenesis. *Nature* **593**:435–439. doi:10.1038/S41586-021-03510-6

Koch A, Thiemann M, Grabenbauer M, Yoon Y, McNiven MA, Schrader M. 2003. Dynamin-like protein 1 is involved in peroxisomal fission. *J Biol Chem* **278**:8597–8605. doi:10.1074/JBC.M211761200

Koch J, Brocard C. 2012. PEX11 proteins attract Mff and human Fis1 to coordinate peroxisomal fission. *Journal of Cell Science* **125**:3813–3826. doi:10.1242/JCS.102178/263234/AM/PEX11-PROTEINS-ATTRACT-MFF-AND-HFIS1-TO-COORDINATE

Kondadi AK, Anand R, Hänsch S, Urbach J, Zobel T, Wolf DM, Segawa M, Liesa M, Shirihai OS, Weidtkamp-Peters S, Reichert AS. 2020. Cristae undergo continuous cycles of membrane remodelling in a MICOS-dependent manner. *EMBO Rep* **21**:e49776. doi:10.15252/EMBR.201949776

Krahenbuhl S, Chang M, Brass EP, Hoppel CL. 1991. Decreased activities of ubiquinol:ferricytochrome c oxidoreductase (complex III) and ferrocytochrome c:oxygen oxidoreductase (complex IV) in liver mitochondria from rats with hydroxycobalamin[c-

878 lactam]-induced methylmalonic aciduria. *Journal of Biological Chemistry* **266**:20998–
879 21003. doi:10.1016/S0021-9258(18)54810-9

880 Lam J, Katti P, Biete M, Mungai M, Ashshareef S, Neikirk K, Lopez EG, Vue Z, Christensen
881 TA, Beasley HK, Rodman TA, Murray SA, Salisbury JL, Glancy B, Shao J, Pereira RO,
882 Abel ED, Hintonjr. A. 2021. A Universal Approach to Analyzing Transmission Electron
883 Microscopy with ImageJ. *Cells 2021, Vol 10, Page 2177* **10**:2177.
884 doi:10.3390/CELLS10092177

885 Lee YJ, Jeong SY, Karbowski M, Smith CL, Youle RJ. 2004. Roles of the mammalian
886 mitochondrial fission and fusion mediators Fis1, Drp1, and Opa1 in apoptosis. *Mol Biol*
887 *Cell* **15**:5001–5011. doi:10.1091/MBC.E04-04-0294

888 Lewis SC, Uchiyama LF, Nunnari J. 2016. ER-mitochondria contacts couple mtDNA
889 synthesis with Mitochondrial division in human cells. *Science (1979)* **353**.
890 doi:10.1126/SCIENCE.AAF5549

891 Li L, Conradson DM, Bharat V, Kim MJ, Hsieh CH, Minhas PS, Papakyrikos AM, Durairaj
892 AS, Ludlam A, Andreasson KI, Partridge L, Cianfrocco MA, Wang X. 2021. A
893 mitochondrial membrane-bridging machinery mediates signal transduction of
894 intramitochondrial oxidation. *Nat Metab* **3**:1242–1258. doi:10.1038/S42255-021-00443-
895 2

896 Li S, Xu S, Roelofs BA, Boyman L, Jonathan Lederer W, Sesaki H, Karbowski M. 2015.
897 Transient assembly of F-actin on the outer mitochondrial membrane contributes to
898 mitochondrial fission. *Journal of Cell Biology* **208**:109–123. doi:10.1083/jcb.201404050

899 Liu Xingmiao, Zhang Z, Li D, Lei M, Li Q, Liu Xiaojun, Zhang P. 2021. DNM1L-Related
900 Mitochondrial Fission Defects Presenting as Encephalopathy: A Case Report and
901 Literature Review. *Front Pediatr* **9**. doi:10.3389/FPED.2021.626657

902 Lodhi IJ, Semenkovich CF. 2014. Peroxisomes: a nexus for lipid metabolism and cellular
903 signaling. *Cell Metab* **19**:380–392. doi:10.1016/J.CMET.2014.01.002

904 Longo F, Benedetti S, Zambon AA, Sora MGN, Di Resta C, De Ritis D, Quattrini A, Maltecca
905 F, Ferrari M, Previtali SC. 2020. Impaired turnover of hyperfused mitochondria in severe
906 axonal neuropathy due to a novel DRP1 mutation. *Hum Mol Genet* **29**:177–188.
907 doi:10.1093/HMG/DDZ211

908 Losó n OC, Song Z, Chen H, Chan DC. 2013. Fis1, Mff, MiD49, and MiD51 mediate Drp1
909 recruitment in mitochondrial fission. *Mol Biol Cell* **24**:659–667. doi:10.1091/MBC.E12-
910 10-0721

911 Martinou JC, Youle RJ. 2006. Which came first, the cytochrome c release or the
912 mitochondrial fission? *Cell Death Differ* **13**:1291–1295. doi:10.1038/SJ.CDD.4401985

913 Montecinos-Franjola F, Bauer BL, Mears JA, Ramachandran R. 2020. GFP fluorescence
914 tagging alters dynamin-related protein 1 oligomerization dynamics and creates
915 disassembly-refractory puncta to mediate mitochondrial fission. *Scientific Reports 2020*
916 *10:1* **10**:1–16. doi:10.1038/s41598-020-71655-x

917 Nagashima S, Tábara LC, Tilokani L, Paupe V, Anand H, Pogson JH, Zunino R, McBride
918 HM, Prudent J. 2020. Golgi-derived PI(4)P-containing vesicles drive late steps of
919 mitochondrial division. *Science (1979)* **367**:1366–1371. doi:10.1126/science.aax6089

920 Nasca A, Legati A, Baruffini E, Nolli C, Moroni I, Ardissone A, Goffrini P, Ghezzi D. 2016.
921 Biallelic Mutations in DNM1L are Associated with a Slowly Progressive Infantile
922 Encephalopathy. *Human Mutation* **37**:898–903. doi:10.1002/HUMU.23033

923 Nolan DA, Chen B, Michon AM, Salatka E, Arndt D. 2019. A Rasmussen encephalitis,
924 autoimmune encephalitis, and mitochondrial disease mimicker: expanding the *DNM1L*-
925 associated intractable epilepsy and encephalopathy phenotype. *Epileptic Disorders*
926 **21**:112–116. doi:10.1684/EPD.2019.1036

927 Osellame LD, Singh AP, Stroud DA, Palmer CS, Stojanovski D, Ramachandran R, Ryan MT.
928 2016. Cooperative and independent roles of the Drp1 adaptors Mff, MiD49 and MiD51
929 in mitochondrial fission. *Journal of Cell Science* **129**:2170–2181.
930 doi:10.1242/JCS.185165/-/DC1

931 Otera H, Miyata N, Kuge O, Mihara K. 2016. Drp1-dependent mitochondrial fission via
932 MiD49/51 is essential for apoptotic cristae remodeling. *Journal of Cell Biology* **212**:531–
933 544. doi:10.1083/jcb.201508099

934 Palmer CS, Elgass KD, Parton RG, Osellame LD, Stojanovski D, Ryan MT. 2013. Adaptor
935 proteins MiD49 and MiD51 can act independently of Mff and Fis1 in Drp1 recruitment
936 and are specific for mitochondrial fission. *J Biol Chem* **288**:27584–27593.
937 doi:10.1074/JBC.M113.479873

938 Prigione A, Adjaye J. 2011. Modulation of mitochondrial biogenesis and bioenergetic
939 metabolism upon in vitro and in vivo differentiation of human ES and iPS cells.
940 *International Journal of Developmental Biology*. doi:10.1387/ijdb.103198ap

941 Rasmussen ML, Taneja N, Neininger AC, Wang L, Robertson GL, Riffle SN, Shi L,
942 Knollmann BC, Burnette DT, Gama V. 2020. MCL-1 Inhibition by Selective BH3
943 Mimetics Disrupts Mitochondrial Dynamics Causing Loss of Viability and Functionality
944 of Human Cardiomyocytes. *iScience* **23**. doi:10.1016/j.isci.2020.101015

945 Ravi A, Palamiuc L, Loughran RM, Triscott J, Arora GK, Kumar A, Tieu V, Pauli C, Reist M,
946 Lew RJ, Houlihan SL, Fellmann C, Metallo C, Rubin MA, Emerling BM. 2021. PI5P4Ks
947 drive metabolic homeostasis through peroxisome-mitochondria interplay. *Dev Cell*
948 **56**:1661-1676.e10. doi:10.1016/J.DEVCEL.2021.04.019

949 Ryan CS, Fine AL, Cohen AL, Schiltz BM, Renaud DL, Wirrell EC, Patterson MC, Boczek
950 NJ, Liu R, Babovic-Vuksanovic D, Chan DC, Payne ET. 2018. De Novo DNM1L Variant
951 in a Teenager With Progressive Paroxysmal Dystonia and Lethal Super-refractory
952 Myoclonic Status Epilepticus. *Journal of Child Neurology* **33**:651–658.
953 doi:10.1177/0883073818778203

954 Schrader M, Costello JL, Godinho LF, Azadi AS, Islinger M. 2016. Proliferation and fission
955 of peroxisomes - An update. *Biochim Biophys Acta* **1863**:971–983.
956 doi:10.1016/J.BBAMCR.2015.09.024

957 Schrader M, Kamoshita M, Islinger M. 2020. Organelle interplay-peroxisome interactions in
958 health and disease. *J Inherit Metab Dis* **43**:71–89. doi:10.1002/JIMD.12083

959 Sheffer R, Douiev L, Edvardson S, Shaag A, Tamimi K, Soiferman D, Meiner V, Saada A.
960 2016. Postnatal microcephaly and pain insensitivity due to a de novo heterozygous
961 DNM1L mutation causing impaired mitochondrial fission and function. *American Journal*
962 *of Medical Genetics, Part A* **170**:1603–1607. doi:10.1002/AJMG.A.37624

963 Smaili SS, Hsu YT, Sanders KM, Russell JT, Youle RJ. 2001. Bax translocation to
964 mitochondria subsequent to a rapid loss of mitochondrial membrane potential. *Cell*
965 *Death Differ* **8**:909–920. doi:10.1038/SJ.CDD.4400889

966 Smirnova E, Griparic L, Shurland DL, van der Bliek AM. 2001. Dynamin-related protein Drp1
967 is required for mitochondrial division in mammalian cells. *Mol Biol Cell* **12**:2245–56.
968 doi:10.1091/mbc.12.8.2245

969 Spinelli JB, Rosen PC, Sprenger H-G, Puszynska AM, Mann JL, Roessler JM, Cangelosi
970 AL, Henne A, Condon KJ, Zhang T, Kunchok T, Lewis CA, Chandel NS, Sabatini DM.
971 2021. Fumarate is a terminal electron acceptor in the mammalian electron transport
972 chain. *Science* **374**:1227–1237. doi:10.1126/SCIENCE.ABI7495

973 Sugiura A, Mattie S, Prudent J, Mcbride HM. 2017. Newly born peroxisomes are a hybrid of
974 mitochondrial and ER-derived pre-peroxisomes. *Nature* **542**:251–254.
975 doi:10.1038/NATURE21375

976 Taguchi N, Ishihara N, Jofuku A, Oka T, Mihara K. 2007. Mitotic phosphorylation of dynamin-
977 related GTPase Drp1 participates in mitochondrial fission. *Journal of Biological*
978 *Chemistry* **282**:11521–11529. doi:10.1074/jbc.M607279200

979 Tanaka H, Okazaki T, Aoyama S, Yokota M, Koike M, Okada Y, Fujiki Y, Gotoh Y. 2019.
980 Peroxisomes control mitochondrial dynamics and the mitochondrion-dependent
981 apoptosis pathway. *J Cell Sci* **132**. doi:10.1242/JCS.224766

982 Theart RP, Kriel J, Toit A du, Loos B, Niesler TR. 2020. Mitochondrial event localiser (MEL)
983 to quantitativelydescribe fission, fusion and depolarisation in the three-dimensional
984 space. *PLOS ONE* **15**:e0229634. doi:10.1371/JOURNAL.PONE.0229634

985 Valera-Alberni M, Joffraud M, Miro-Blanch J, Capellades J, Junza A, Dayon L, Núñez
986 Galindo A, Sanchez-Garcia JL, Valsesia A, Cercillieux A, Söllner F, Ladurner AG,
987 Yanes O, Cantó C. 2021. Crosstalk between Drp1 phosphorylation sites during
988 mitochondrial remodeling and their impact on metabolic adaptation. *Cell Reports* **36**.
989 doi:10.1016/J.CELREP.2021.109565/ATTACHMENT/3EF18C2E-C1FE-434A-A87F-
990 E1E1BD407021/MMC1.PDF

991 Vandeleur D, Chen C V., Huang EJ, Connolly AJ, Sanchez H, Moon-Grady AJ. 2019. Novel
992 and lethal case of cardiac involvement in DNM1L mitochondrial encephalopathy.
993 *American Journal of Medical Genetics, Part A* **179**:2486–2489.
994 doi:10.1002/AJMG.A.61371

995 Vantaggiato C, Castelli M, Giovarelli M, Orso G, Bassi MT, Clementi E, De Palma C. 2019.
996 The Fine Tuning of Drp1-Dependent Mitochondrial Remodeling and Autophagy

997 Controls Neuronal Differentiation. *Frontiers in Cellular Neuroscience* **13**:120.
998 doi:10.3389/fncel.2019.00120

999 Vincent AE, White K, Davey T, Philips J, Ogden RT, Lawess C, Warren C, Hall MG, Ng YS,
1000 Falkous G, Holden T, Deehan D, Taylor RW, Turnbull DM, Picard M. 2019. Quantitative
1001 3D Mapping of the Human Skeletal Muscle Mitochondrial Network. *Cell Reports* **26**:996-
1002 1009.e4. doi:10.1016/J.CELREP.2019.01.010/ATTACHMENT/FB7711C2-65A0-4155-
1003 8EB8-6FD4440E627D/MMC1.PDF

1004 Wai T, Langer T. 2016. Mitochondrial Dynamics and Metabolic Regulation. *Trends in*
1005 *Endocrinology and Metabolism*. doi:10.1016/j.tem.2015.12.001

1006 Wakabayashi J, Zhang Z, Wakabayashi N, Tamura Y, Fukaya M, Kensler TW, Iijima M,
1007 Sesaki H. 2009. The dynamin-related GTPase Drp1 is required for embryonic and brain
1008 development in mice. *Journal of Cell Biology* **186**:805–816. doi:10.1083/jcb.200903065

1009 Wasiak S, Zunino R, McBride HM. 2007. Bax/Bak promote sumoylation of DRP1 and its
1010 stable association with mitochondria during apoptotic cell death. *J Cell Biol* **177**:439–
1011 450. doi:10.1083/JCB.200610042

1012 Wasilewski M, Chacinska A. 2021. MIC60 relays oxidation to block mitophagy. *Nature*
1013 *Metabolism 2021 3:9* **3**:1146–1147. doi:10.1038/s42255-021-00460-1

1014 Waterham HR, Ferdinandusse S, Wanders RJA. 2016. Human disorders of peroxisome
1015 metabolism and biogenesis. *Biochimica et Biophysica Acta (BBA) - Molecular Cell*
1016 *Research* **1863**:922–933. doi:10.1016/J.BBAMCR.2015.11.015

1017 Waterham HR, Koster J, van Roermund CWT, Mooyer PAW, Wanders RJA, Leonard J V.
1018 2007. A lethal defect of mitochondrial and peroxisomal fission. *N Engl J Med* **356**:1736–
1019 1741. doi:10.1056/NEJMOA064436

1020 Whitley BN, Lam C, Cui H, Haude K, Bai R, Escobar L, Hamilton A, Brady L, Tarnopolsky
1021 MA, Dengle L, Picker J, Lincoln S, Lackner LL, Glass IA, Hoppins S. 2018. Aberrant
1022 Drp1-mediated mitochondrial division presents in humans with variable outcomes.
1023 *Human Molecular Genetics* **27**:3710–3719. doi:10.1093/hmg/ddy287

1024 Wilkens V, Kohl W, Busch K. 2013. Restricted diffusion of OXPHOS complexes in dynamic
1025 mitochondria delays their exchange between cristae and engenders a transitory mosaic
1026 distribution. *J Cell Sci* **126**:103–116. doi:10.1242/JCS.108852

1027 Ye F, Hoppel CL. 2013. Measuring oxidative phosphorylation in human skin fibroblasts. *Anal*
1028 *Biochem* **437**:52–58. doi:10.1016/J.AB.2013.02.010

1029 Yoon G, Malam Z, Paton T, Marshall CR, Hyatt E, Ivakine Z, Scherer SW, Lee KS, Hawkins
1030 C, Cohn RD. 2016. Lethal Disorder of Mitochondrial Fission Caused by Mutations in
1031 DNM1L. *The Journal of Pediatrics* **171**:313-316.e2. doi:10.1016/J.JPEDS.2015.12.060

1032

Figure 1

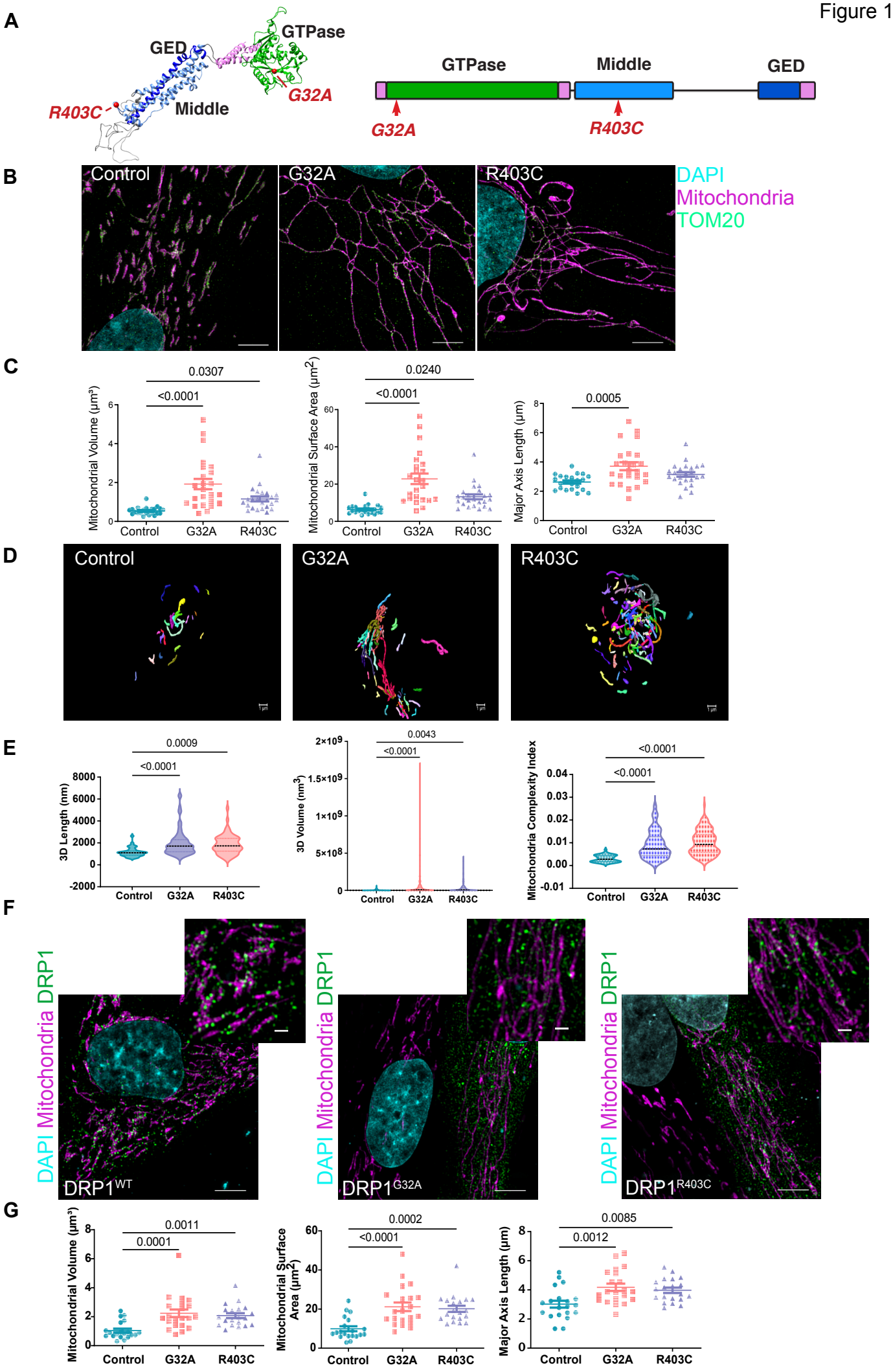
A
GED
GTPase
G32A
R403C
Middle
GTPase
Middle
GED
G32A
R403C
B
Control
G32A
R403C
DAPI
Mitochondria
TOM20
C
Mitochondrial Volume (µm³)
0.0307
<0.0001
Control
G32A
R403C
Mitochondrial Surface Area (µm²)
0.0240
<0.0001
Major Axis Length (µm)
0.0005
D
Control
G32A
R403C
E
3D Length (nm)
0.0009
<0.0001
3D Volume (nm³)
0.0043
<0.0001
Mitochondria Complexity Index
<0.0001
<0.0001
F
DAPI Mitochondria DRP1
DRP1WT
DRP1G32A
DRP1R403C
G
Mitochondrial Volume (µm³)
0.0011
0.0001
Mitochondrial Surface Area (µm²)
0.0002
<0.0001
Major Axis Length (µm)
0.0085
0.0012

Figure 2

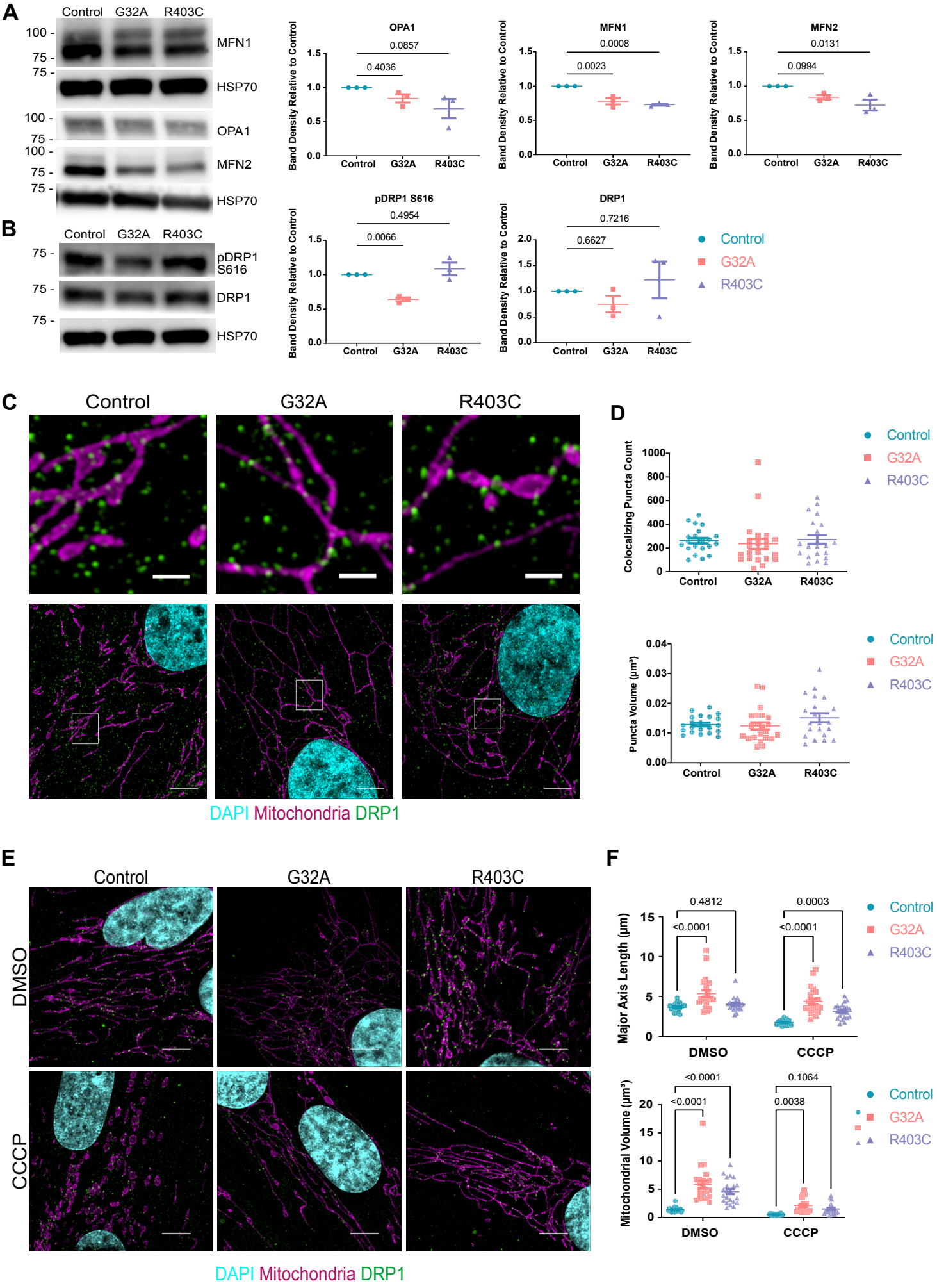
A
Control G32A R403C
100 -
75 -
MFN1
HSP70
OPA1
MFN2
B
pDRP1 S616
DRP1
Band Density Relative to Control
OPA1
0.0857
0.4036
MFN1
0.0008
0.0023
MFN2
0.0131
0.0994
pDRP1 S616
0.4954
0.0066
DRP1
0.7216
0.6627
Control
G32A
R403C
C
Control
G32A
R403C
DAPI Mitochondria DRP1
D
Colocalizing Puncta Count
Puncta Volume (μm³)
E
DMSO
CCCP
DAPI Mitochondria DRP1
F
Major Axis Length (μm)
0.4812
<0.0001
0.0003
<0.0001
Mitochondrial Volume (μm³)
<0.0001
<0.0001
0.1064
0.0038
DMSO
CCCP

Figure 3

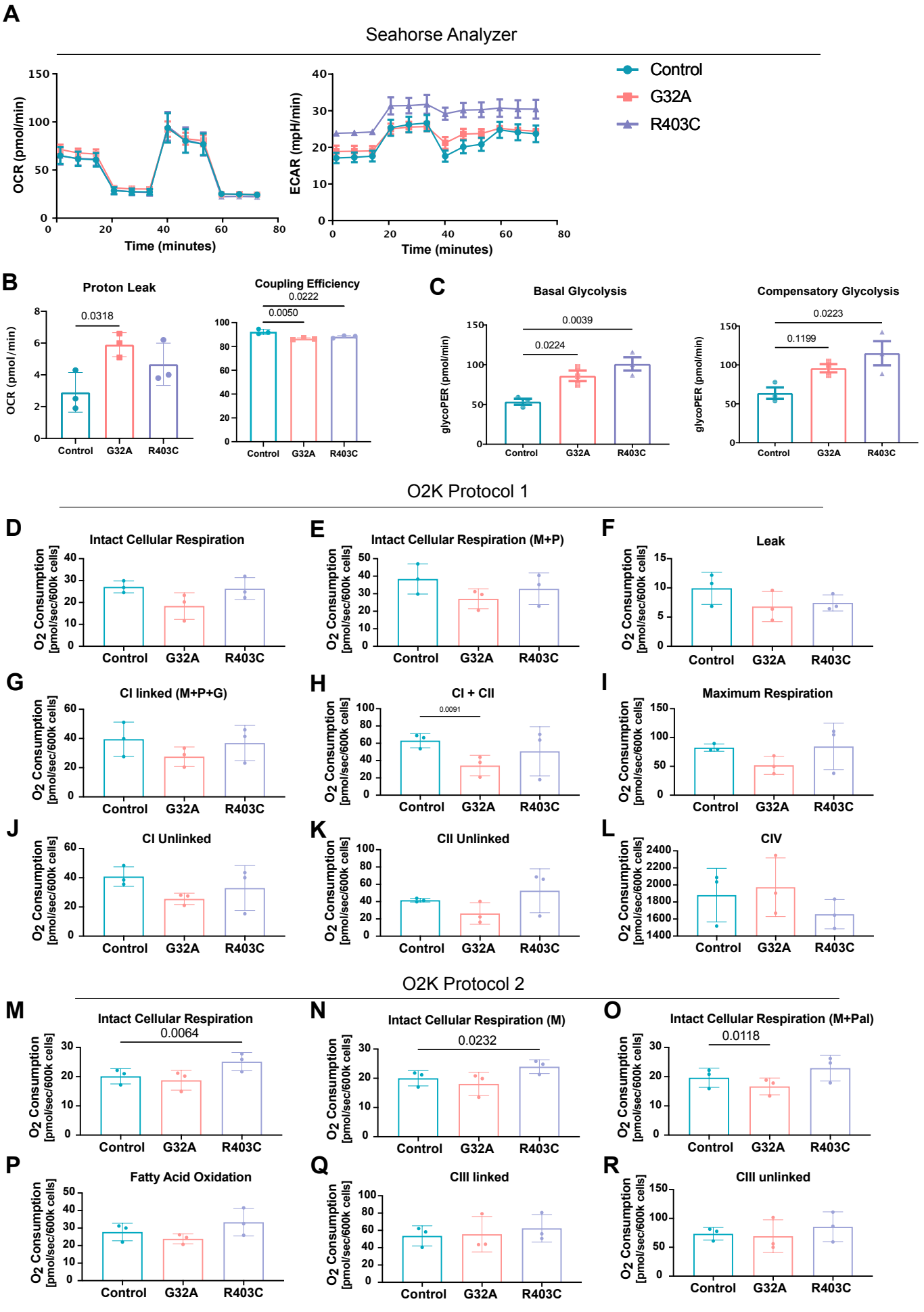
A
Seahorse Analyzer
OCR (pmol/min)
Time (minutes)
ECAR (mpH/min)
Control
G32A
R403C
B
Proton Leak
0.0318
Coupling Efficiency
0.0222
0.0050
C
Basal Glycolysis
0.0039
0.0224
Compensatory Glycolysis
0.0223
0.1199
glycoPER (pmol/min)
O2K Protocol 1
D
Intact Cellular Respiration
E
Intact Cellular Respiration (M+P)
F
Leak
G
CI linked (M+P+G)
H
CI + CII
0.0091
I
Maximum Respiration
J
CI Unlinked
K
CII Unlinked
L
CIV
O2 Consumption [pmol/sec/600k cells]
O2K Protocol 2
M
Intact Cellular Respiration
0.0064
N
Intact Cellular Respiration (M)
0.0232
O
Intact Cellular Respiration (M+Pal)
0.0118
P
Fatty Acid Oxidation
Q
CIII linked
R
CIII unlinked

Figure 4

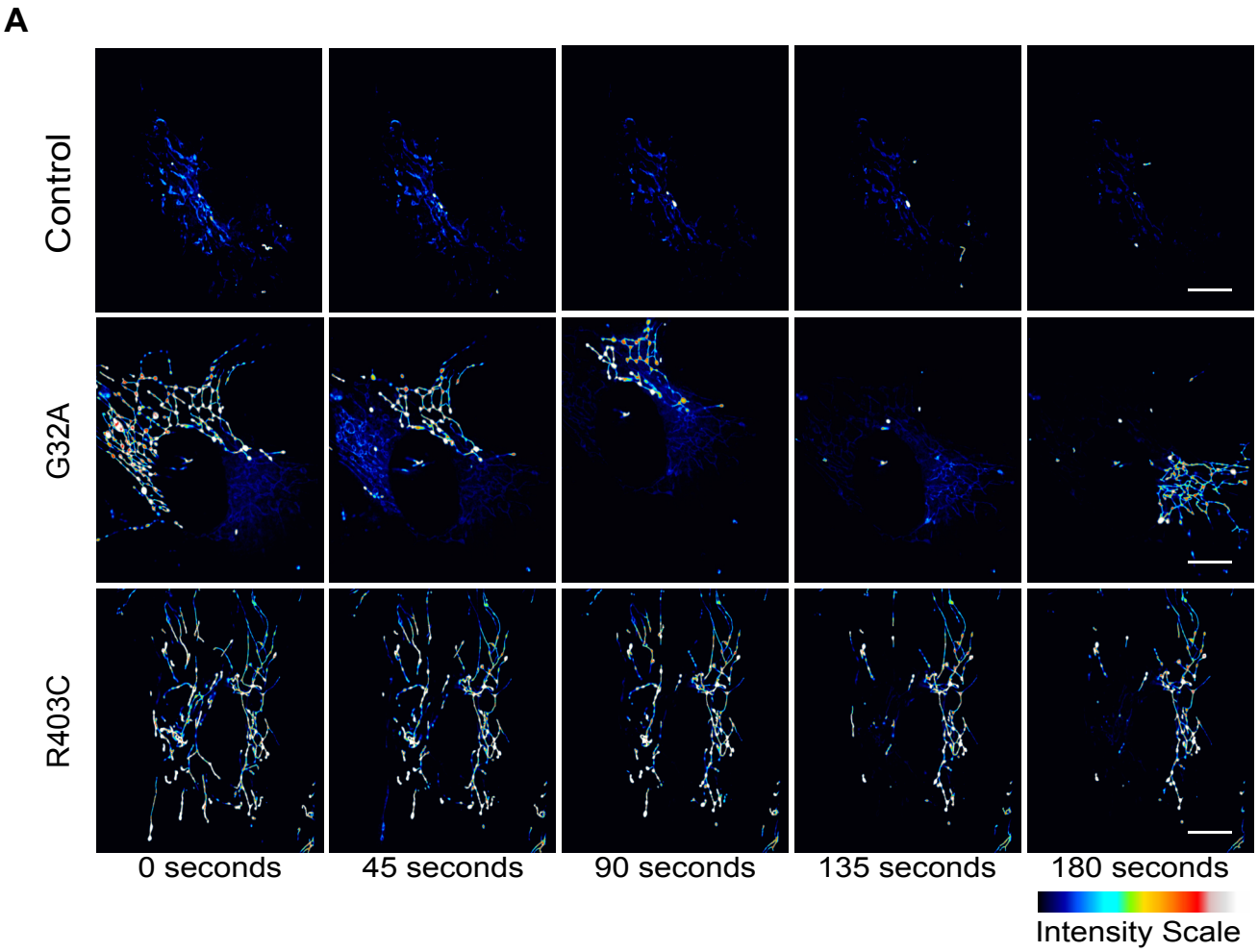
A
Control
G32A
R403C
0 seconds
45 seconds
90 seconds
135 seconds
180 seconds
Intensity Scale

Figure 5

A

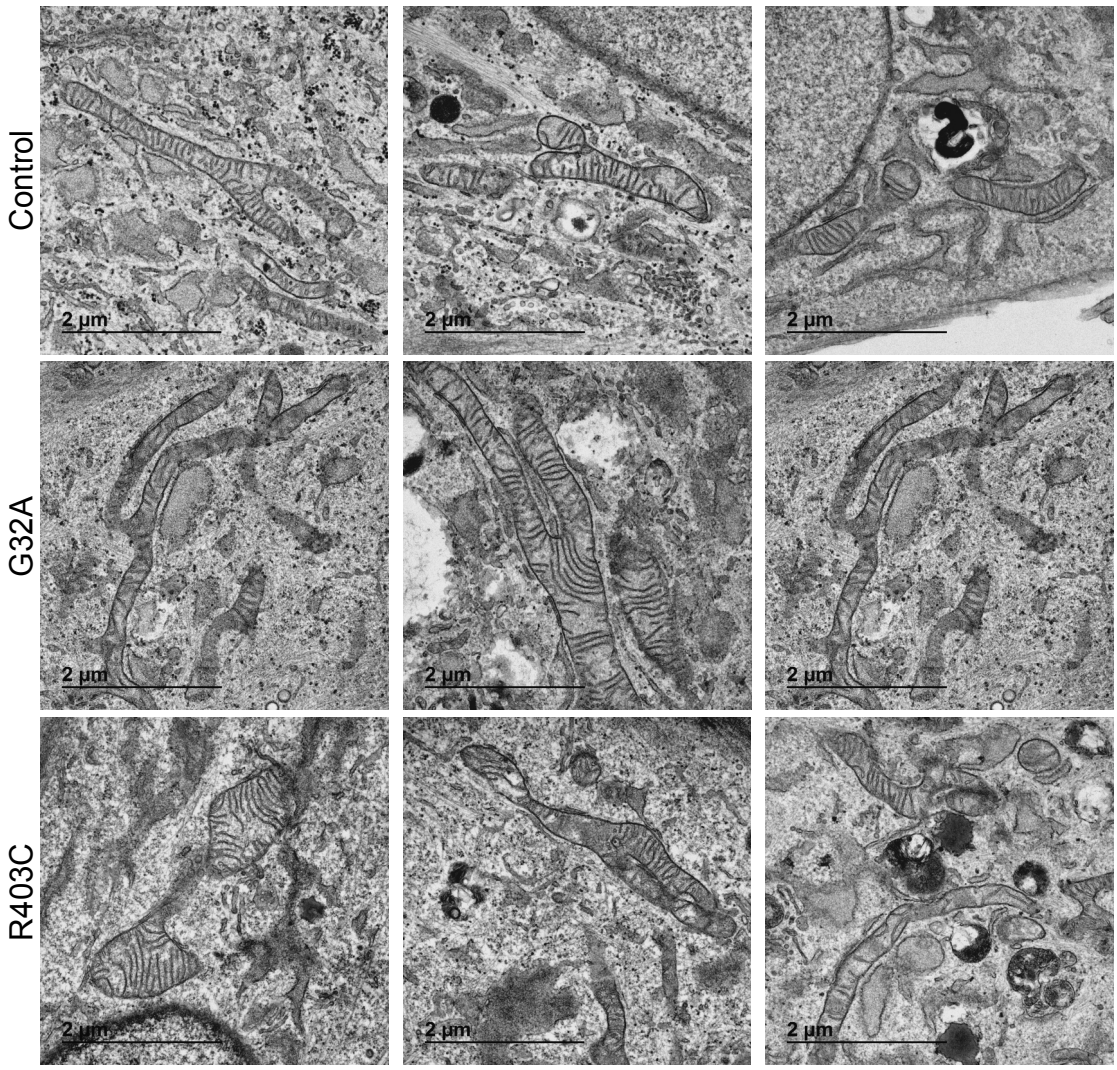
Control
G32A
R403C
2 µm

B

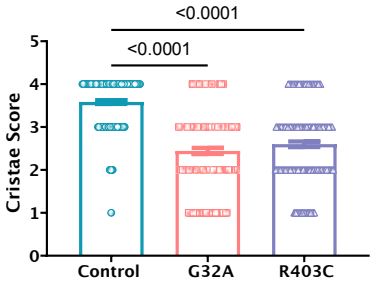
<0.0001
<0.0001
Cristae Score
0
1
2
3
4
5
Control
G32A
R403C

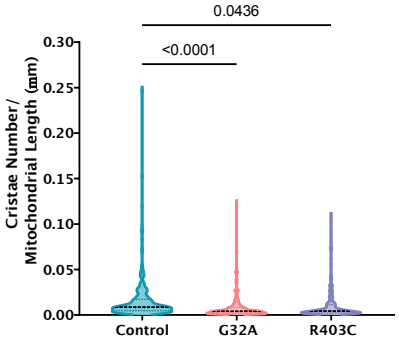
0.0436
<0.0001
Cristae Number/
Mitochondrial Length (µm)
0.00
0.05
0.10
0.15
0.20
0.25
0.30
Control
G32A
R403C

Figure 6

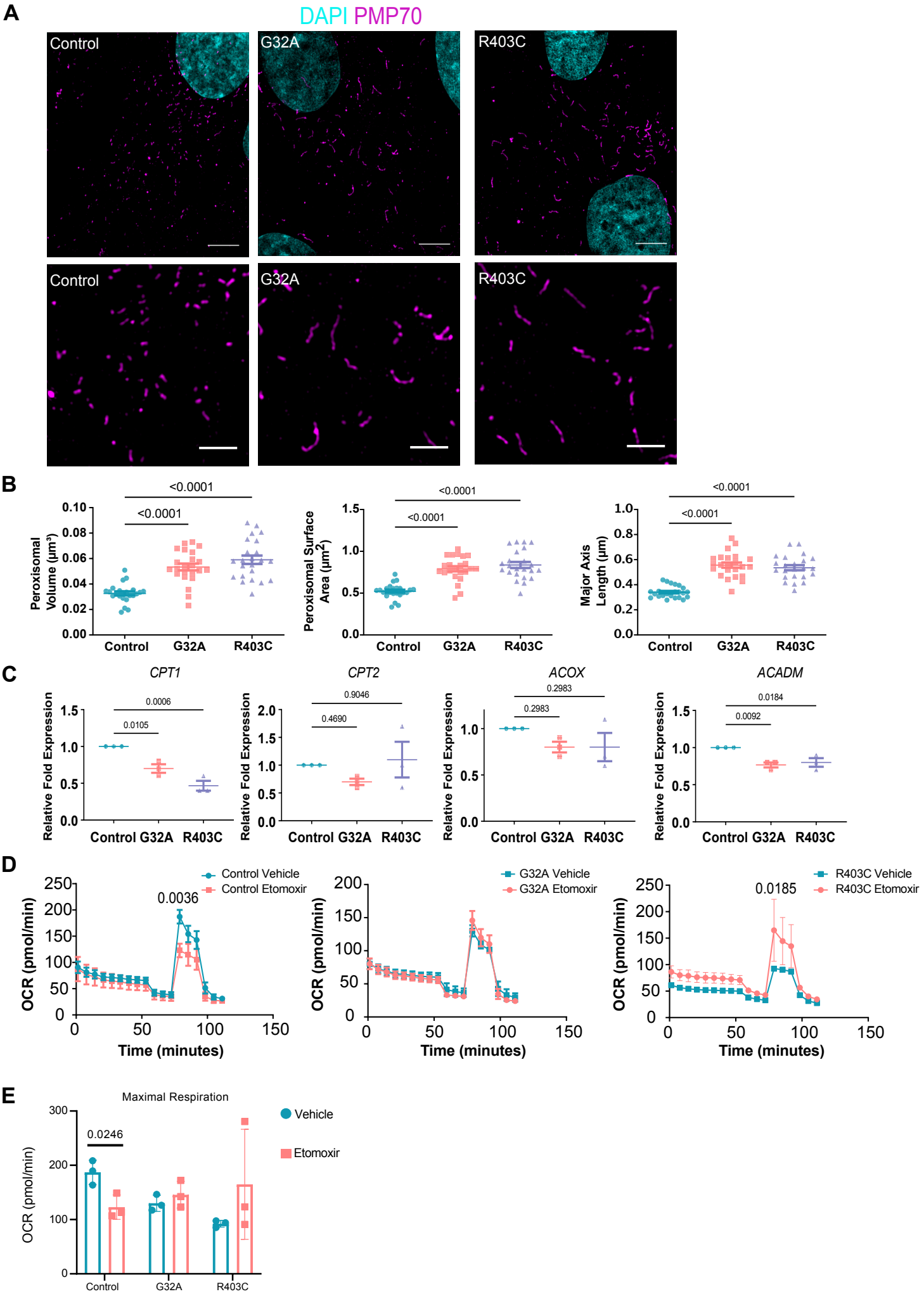
A
DAPI PMP70
Control
G32A
R403C
B
Peroxisomal Volume (µm³)
Peroxisomal Surface Area (µm²)
Major Axis Length (µm)
<0.0001
Control
G32A
R403C
C
CPT1
CPT2
ACOX
ACADM
Relative Fold Expression
0.0006
0.0105
0.9046
0.4690
0.2983
0.2983
0.0184
0.0092
D
Control Vehicle
Control Etomoxir
G32A Vehicle
G32A Etomoxir
R403C Vehicle
R403C Etomoxir
0.0036
0.0185
OCR (pmol/min)
Time (minutes)
E
Maximal Respiration
0.0246
Vehicle
Etomoxir
OCR (pmol/min)
Control
G32A
R403C

Figure 7

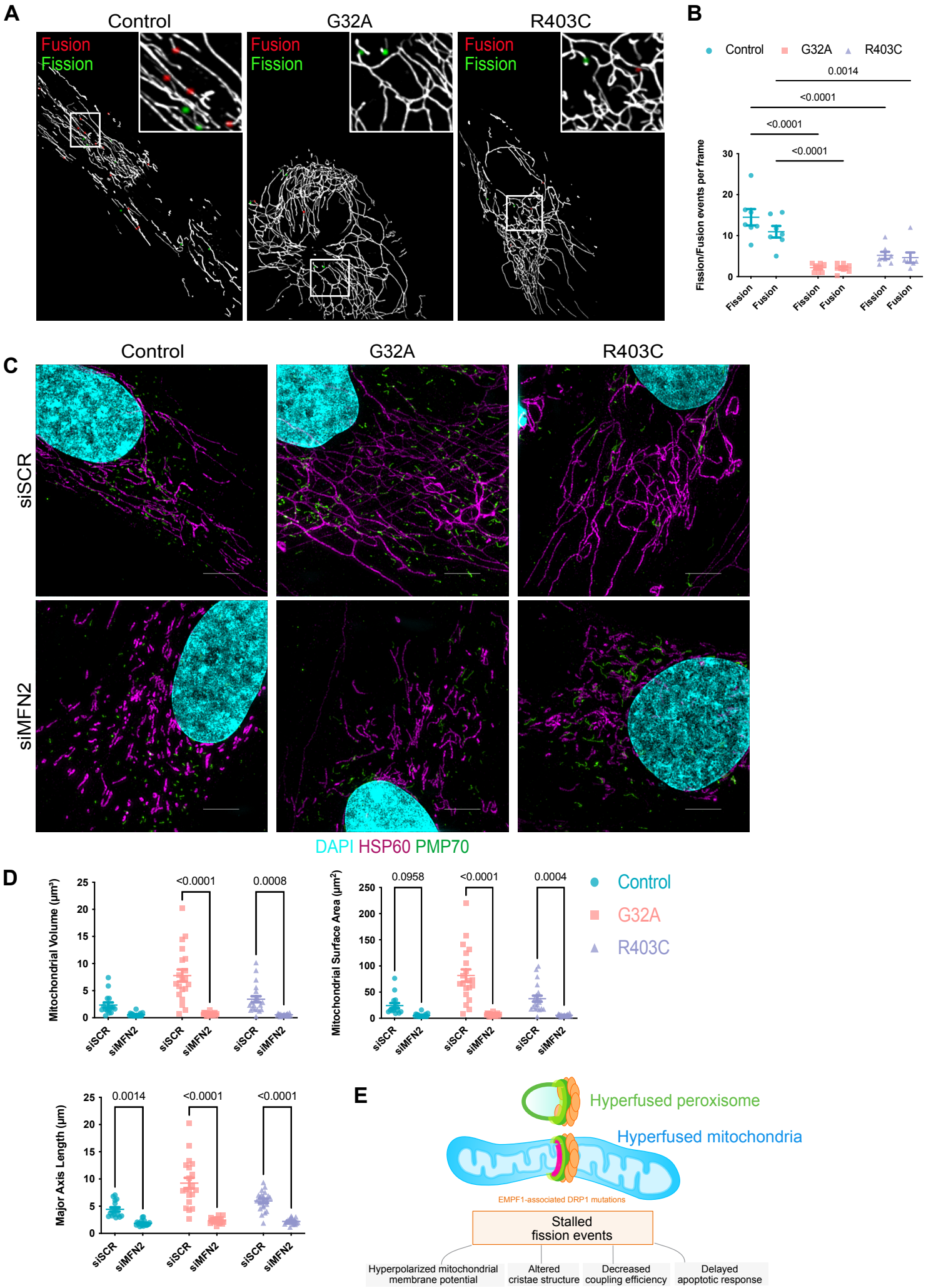
A
Control
G32A
R403C
Fusion
Fission
B
Control
G32A
R403C
0.0014
<0.0001
<0.0001
<0.0001
Fission/Fusion events per frame
30
20
10
0
Fission
Fusion
Fission
Fusion
Fission
Fusion
C
Control
G32A
R403C
siSCR
siMFN2
DAPI HSP60 PMP70
D
Mitochondrial Volume (µm³)
<0.0001
0.0008
Mitochondrial Surface Area (µm²)
0.0958
<0.0001
0.0004
Control
G32A
R403C
siSCR
siMFN2
Major Axis Length (µm)
0.0014
<0.0001
<0.0001
E
Hyperfused peroxisome
Hyperfused mitochondria
EMPF1-associated DRP1 mutations
Stalled fission events
Hyperpolarized mitochondrial membrane potential
Altered cristae structure
Decreased coupling efficiency
Delayed apoptotic response